library plasmid from 77 of these. Fifty-one of these 77 clones were sequenced and found to encode Tbx6.

EMSA. The full-length Tbx6 ORF was obtained from the pACT-Tbx6 construct, which was isolated from the yeast one-hybrid screening. After ligation to a 3XFLAG tag (Sigma), the tagged Tbx6 insert was cloned into pCS2+ (46). *In vitro* transcription/translation was then performed with a TNT *in vitro* translation kit (Promega) following the manufacturer's protocol. Oligonucleotide probes were labeled with digoxigenin-11-dideoxy UTP by using recombinant TdT (Roche Diagnostics). Crude *in vitro* translated product (5 μl) was subjected to EMSA as a protein sample. As a negative control, reticulocyte lysate without Tbx6 template was used. EMSA was performed by using the DIG Gel Shift Kit, 2nd Generation (Roche Diagnostics), following the manufacturer's protocol. The band shifts were detected by using LumiImager LAS-1000 (Fuji).

Luciferase Assay. Segments (356 bp) corresponding to the 5′-adjoining sequence of the *Mesp2* ORF, with and without mutations in the conserved binding sites, were subcloned into the pGL3-Basic (Promega) vector to generate luciferase reporter constructs. The expression vectors for the proteins to be assessed were constructed in the same way as that used in the EMSAs described above. COS-7 cells were routinely and regularly passaged in DMEM supplemented with 10% FBS. Cells were seeded at 2.5×10^4 cells per well in 24-well plates, and, after 24 h of cultivation, they were transfected with a total of 350 ng of DNA containing the reporter plasmids and expression vectors for the proteins under analysis (50 ng of each expression vector and 200 ng of reporter construct, adjusted to 350 ng by the addition of empty vector). Twenty-four hours after transfection, the cells were lysed by Passive Lysis Buffer (Promega) and subjected to a luciferase assay by using the Dual Luciferase System (Promega). In all experiments, 5 ng of the sea pansy luciferase expression vector phRL-TK (Promega) was used per well as the internal control. Luciferase activity was normalized to the phRL-TK internal control activity (sea pansy luciferase). The experiments were performed in triplicate for each assay and repeated at least twice.

We are grateful to Tasuku Honjo (Kyoto University, Kyoto) for providing cDNA clones of RBPJκ, RBPJκ-VP16, and dnRBPJκ (R218H) and to Mariko Ikumi, Eriko Ikeno, and Shinobu Watanabe for technical assistance. We also thank Hiroyuki Takeda, Mitsuru Morimoto, and Masayuki Oginuma for helpful discussions and for their comments on the manuscript. This work was supported by the Organized Research Combination System of the Ministry of Education, Culture, Sports, Science, and Technology, Japan.

1. Huppert, S. S., Ilagan, M. X., De Strooper, B. & Kopan, R. (2005) *Dev. Cell* **8,** 677–688.
2. Morimoto, M., Takahashi, Y., Endo, M. & Saga, Y. (2005) *Nature* **435,** 354–359.
3. Bessho, Y., Hirata, H., Masamizu, Y. & Kageyama, R. (2003) *Genes Dev.* **17,** 1451–1456.
4. Aulehla, A., Wehrle, C., Brand-Saberi, B., Kemler, R., Gossler, A., Kanzler, B. & Herrmann, B. G. (2003) *Dev. Cell* **4,** 395–406.
5. Sawada, A., Shinya, M., Jiang, Y. J., Kawakami, A., Kuroiwa, A. & Takeda, H. (2001) *Development* **128,** 4873–4880.
6. Moreno, T. A. & Kintner, C. (2004) *Dev. Cell* **6,** 205–218.
7. Chapman, D. L. & Papaioannou, V. E. (1998) *Nature* **391,** 695–697.
8. Saga, Y., Hata, N., Koseki, H. & Taketo, M. M. (1997) *Genes Dev.* **11,** 1827–1839.
9. Takahashi, Y., Koizumi, K., Takagi, A., Kitajima, S., Inoue, T., Koseki, H. & Saga, Y. (2000) *Nat. Genet.* **25,** 390–396.
10. Takahashi, Y., Inoue, T., Gossler, A. & Saga, Y. (2003) *Development* **130,** 4259–4268.
11. Haraguchi, S., Kitajima, S., Takagi, A., Takeda, H., Inoue, T. & Saga, Y. (2001) *Mech. Dev.* **108,** 59–69.
12. Conlon, F. L., Fairclough, L., Price, B. M., Casey, E. S. & Smith, J. C. (2001) *Development* **128,** 3749–3758.
13. Mitani, Y., Takahashi, H. & Satoh, N. (2001) *Development* **128,** 3717–3728.
14. Muller, C. W. & Herrmann, B. G. (1997) *Nature* **389,** 884–888.
15. Wilson, V. & Conlon, F. L. (2002) *Genome Biol.* **3,** REVIEWS3008.
16. Kraus, F., Haenig, B. & Kispert, A. (2001) *Mech. Dev.* **100,** 83–86.
17. Koseki, H., Wallin, J., Wilting, J., Mizutani, Y., Kispert, A., Ebensperger, C., Herrmann, B. G., Christ, B. & Balling, R. (1993) *Development* **119,** 649–660.
18. Hurlin, P. J., Steingrimsson, E., Copeland, N. G., Jenkins, N. A. & Eisenman, R. N. (1999) *EMBO J.* **18,** 7019–7028.
19. Lardelli, M. (2003) *Dev. Genes Evol.* **213,** 519–522.
20. White, P. H. & Chapman, D. L. (2005) *Genesis* **42,** 193–202.
21. Nikaido, M., Kawakami, A., Sawada, A., Furutani-Seiki, M., Takeda, H. & Araki, K. (2002) *Nat. Genet.* **31,** 195–199.
22. Davidson, B., Shi, W. & Levine, M. (2005) *Development* **132,** 4811–4818.
23. Chapman, D. L., Agulnik, I., Hancock, S., Silver, L. M. & Papaioannou, V. E. (1996) *Dev. Biol.* **180,** 534–542.
24. Mumm, J. S. & Kopan, R. (2000) *Dev. Biol.* **228,** 151–165.
25. Furriols, M. & Bray, S. (2000) *Dev. Biol.* **227,** 520–532.
26. Jarriault, S., Brou, C., Logeat, F., Schroeter, E. H., Kopan, R. & Israel, A. (1995) *Nature* **377,** 355–358.
27. Barolo, S., Walker, R. G., Polyanovsky, A. D., Freschi, G., Keil, T. & Posakony, J. W. (2000) *Cell* **103,** 957–969.
28. Matsuno, K., Go, M. J., Sun, X., Eastman, D. S. & Artavanis-Tsakonas, S. (1997) *Development* **124,** 4265–4273.
29. Hori, K., Fostier, M., Ito, M., Fuwa, T. J., Go, M. J., Okano, H., Baron, M. & Matsuno, K. (2004) *Development* **131,** 5527–5537.
30. Koizumi, K., Nakajima, M., Yuasa, S., Saga, Y., Sakai, T., Kuriyama, T., Shirasawa, T. & Koseki, H. (2001) *Development* **128,** 1391–1402.
31. Kato, H., Taniguchi, Y., Kurooka, H., Minoguchi, S., Sakai, T., Nomura-Okazaki, S., Tamura, K. & Honjo, T. (1997) *Development* **124,** 4133–4141.
32. Schroeter, E. H., Kisslinger, J. A. & Kopan, R. (1998) *Nature* **393,** 382–386.
33. De Strooper, B., Annaert, W., Cupers, P., Saftig, P., Craessaerts, K., Mumm, J. S., Schroeter, E. H., Schrijvers, V., Wolfe, M. S., Ray, W. J., *et al.* (1999) *Nature* **398,** 518–522.
34. Oka, C., Nakano, T., Wakeham, A., de la Pompa, J. L., Mori, C., Sakai, T., Okazaki, S., Kawaichi, M., Shiota, K., Mak, T. W. & Honjo, T. (1995) *Development* **121,** 3291–3301.
35. Dubrulle, J. & Pourquie, O. (2004) *Development* **131,** 5783–5793.
36. Delfini, M. C., Dubrulle, J., Malapert, P., Chal, J. & Pourquie, O. (2005) *Proc. Natl. Acad. Sci. USA* **102,** 11343–11348.
37. Sakai, Y., Meno, C., Fujii, H., Nishino, J., Shiratori, H., Saijoh, Y., Rossant, J. & Hamada, H. (2001) *Genes Dev.* **15,** 213–225.
38. Kawamura, A., Koshida, S., Hijikata, H., Sakaguchi, T., Kondoh, H. & Takada, S. (2005) *Genes Dev.* **19,** 1156–1161.
39. White, P. H., Farkas, D. R. & Chapman, D. L. (2005) *Genesis* **42,** 61–70.
40. White, P. H., Farkas, D. R., McFadden, E. E. & Chapman, D. L. (2003) *Development* **130,** 1681–1690.
41. Hofmann, M., Schuster-Gossler, K., Watabe-Rudolph, M., Aulehla, A., Herrmann, B. G. & Gossler, A. (2004) *Genes Dev.* **18,** 2712–2717.
42. Hogan, B., Beddington, R., Costantini, F. & Lacy, E. (1994) *Manipulating the Mouse Embryo: A Laboratory Manual* (Cold Spring Harbor Lab. Press, Woodbury, NY).
43. Saga, Y., Yagi, T., Ikawa, Y., Sakakura, T. & Aizawa, S. (1992) *Genes Dev.* **6,** 1821–1831.
44. Sasaki, H. & Hogan, B. L. (1996) *Genes Cells* **1,** 59–72.
45. Ohara, O., Nagase, T., Mitsui, G., Kohga, H., Kikuno, R., Hiraoka, S., Takahashi, Y., Kitajima, S., Saga, Y. & Koseki, H. (2002) *DNA Res.* **9,** 47–57.
46. Rupp, R. A., Snider, L. & Weintraub, H. (1994) *Genes Dev.* **8,** 1311–1323.

RESEARCH ARTICLE

Mesp1-Nonexpressing Cells Contribute to the Ventricular Cardiac Conduction System†

Satoshi Kitajima,[1]* Sachiko Miyagawa-Tomita,[2] Tohru Inoue,[3] Jun Kanno,[1] and Yumiko Saga[4]*

Previous fate mapping analysis, using Cre recombinase driven by the *Mesp1* locus, revealed that *Mesp1* is expressed in almost all of the precursors of the cardiovascular system, including the endothelium, endocardium, myocardium, and epicardium. *Mesp1*-nonexpressing cells were found to be restricted to the outflow tract cushion and along the interventricular septum (IVS), which is a location that is suggestive of specialized cardiac conduction system (CCS). In our current study, we examined the identity of these IVS cells by using the pattern of β-galactosidase activity in *CCS-lacZ* mice. In addition, by crossing *Mesp1-Cre* and *floxed GFP reporter* mice with *CCS-lacZ* mice, we have calculated that approximately 20% of the ventricular CCS within the IVS corresponds to *Mesp1*-nonexpressing cells. These data suggest that the ventricular CCS is of heterocellular origin. Furthermore, we indicate a possibility that a population of the cells that contribute to the ventricular CCS might be distinguished at an early stage of development. *Developmental Dynamics 235:395–402, 2006.* © 2005 Wiley-Liss, Inc.

Key words: *Mesp1*; mesoderm; heart differentiation; cardiac conduction system; cell-lineage analysis

Accepted 30 September 2005

INTRODUCTION

The heart is the first functional organ to be formed during organogenesis, and cells that are destined to form cardiac mesoderm are induced both before and during gastrulation. The cells of the cardiac mesoderm invaginate through the primitive streak and migrate with the cranial mesoderm. The bilaterally symmetric cardiac precursors subsequently migrate and converge at the midline of the embryo to form the cardiac crescent, which then forms a linear, single heart tube. The heart tube, formed by an outer myocardium and an inner endocardium, then undergoes rightward looping, which is lined by an acellular matrix (the cardiac jelly). The looped heart tube then undergoes septation to generate a mature, four-chambered cardiac structure in mammals.

The heart is composed of three major cardiac cell types: (1) the endocardium, a part of which forms the cushion tissue by transformation from epithelial to mesenchymal cells; (2) the myocardium; and (3) the epicardium (for review, see Moorman and Christoffels, 2003). The major components of the heart, such as endocardium and myocardium, are of mesodermal origin (i.e., cardiogenic mesoderm), but the contribution of other cell lineages has also been reported for both chick and mouse. Fate mapping of the avian cardiac neural crest has been well documented, and it was reported previously from such

The Supplementary Material referred to in this article can be found at http://www.interscience.wiley.com/jpages/1058-8388/suppmat

† This article was accepted for inclusion in Developmental Dynamics 235#1, January 2006—Cardiovascular Special Issue.

[1] Division of Cellular & Molecular Toxicology, Biological Safety Research Center, National Institute of Health Sciences, Setagaya-ku, Tokyo, Japan
[2]Department of Pediatric Cardiology, The Heart Institute of Japan, Tokyo Women's Medical University, Shinjuku-ku, Tokyo, Japan
[3]Biological Safety Research Center, National Institute of Health Sciences, Setagaya-ku, Tokyo, Japan
[4]Division of Mammalian Development, National Institute of Genetics, Mishima, Japan

Grant sponsor: Ministry of Education, Science, Sports, and Culture in Japan; Grant sponsor: Burroughs–Wellcome Fund Clinical Scientist Award in Translational Research.

***Correspondence to: Yumiko Saga, Ph.D., Division of Mammalian Development, National Institute of Genetics, Yata 1111, Mishima 411-8540, Japan. E-mail: ysaga@lab.nig.ac.jp or Satoshi Kitajima, D.V.M.Ph.D, Division of Cellular & Molecular Toxicology National Institute of Health Sciences, 1-18-1 Kamiyohga, Setagaya-ku, Tokyo 158-8501, Japan. E-mail: satoshi@nihs.go.jp**

DOI 10.1002/dvdy.20640
Published online 29 November 2005 in Wiley InterScience (www.interscience.wiley.com).

experiments using quail–chick chimera that two types of mesenchyme, cardiac neural crest derived and non-neural crest derived, participate in outflow septation and remodeling (Kirby et al., 1983; Waldo et al., 1998). Recently, through the use of the Cre-*loxP* system in mice, it has been demonstrated clearly that the cardiac outflow tract (OT) cushions are contributed in part by cardiac neural crest cells (Yamauchi et al., 1999; Jiang et al., 2000). Additionally, lineage analysis using *Tie2-cre* in mice has suggested that the OT cushions are of mixed origins, containing neural crest cells and endocardium, whereas the atrioventricular (AV) cushions are mainly derived from cells originating from endocardium (Kisanuki et al., 2001).

The specialized cardiac conduction system (CCS) includes the sinoatrial (SA) node, which generates a pacemaker impulse; the AV node, which delays the electrical impulse and allows for the sequential contraction of the atrial and ventricular chambers of the heart; and the ventricular CCS, such as the atrioventricular bundle (AVB), bundle branches, and their ramifications, which facilitates the fast and coordinated conduction of impulses to and throughout the ventricles. Cells in the CCS are characterized by their larger size, reduced number of myofibrils, and large accumulations of glycogen (Mikawa, 1999). It has also been suggested that the CCS might be categorized into two parts based on their origin (Moorman et al., 1998, 2003). One is the SA and AV nodes, which might be derived from the slow-conducting myocardium of the inflow tract and AV canal. The other one is the ventricular CCS, which possibly develops from the trabecular ventricular component. In chick, an elegant series of experiments using retroviral lineage-tracing has provided strong evidence that ventricular components of the conduction system are derived from cardiomyogenic cells (Gourdie et al., 1995; Cheng et al., 1999). In addition, it has been suggested that the differentiation of a subset of Purkinje fibers, adjacent to the arterial bed, might be regulated by local signals from the coronary artery (Gourdie et al., 1995). It was subsequently shown that endothelin-1, a paracrine factor secreted by endothelial cells, is capable of inducing embryonic chick myocytes to the cells of the CCS.

In contrast to the avian CCS, the ventricular CCS in most mammals is morphologically and topologically different from that of chick as it is mainly subendocardial. Hence, the developmental role of the coronary artery in mammalian CCS differentiation is uncertain. In the murine heart, the expression of several markers, including specific connexins and *lacZ* under the transcriptional regulation of either the *minK* or *HF-1b* loci, delineate the bundle branches and proximal Purkinje fibers, but none appear to delineate the full extent of the conductive network along the ventricular free walls (Delorme et al., 1995; Coppen et al., 1998, 1999; Kupershmidt et al., 1999; Nguyen-Tran et al., 2000). In contrast, the entire mouse CCS, including the distal Purkinje fiber network, in both embryonic and neonatal hearts has been visualized recently by way of β-galactosidase (β-gal) reporter activity (Rentschler et al., 2001) in the *CCS-lacZ* mouse line. Recently, the β-gal–positive cells in the interventricular septum (IVS) region of the *CCS-lacZ* adult mice have been reported to correspond to the Cx40-positive cells (Myers and Fishman, 2004). However, the comparison was performed by using serial sections; thus, further clarification is needed to determine whether the same cell expresses the both markers or not. Nevertheless, it is considered that the β-gal–positive cells of *CCS-lacZ* embryos are the most reliable indication for CCS cells in the mouse embryo, compared with the other markers. Although the lineage of the cells of the murine CCS is incompletely characterized, a recent study demonstrated that exogenous treatment of 8.5–10.5 days postcoitum (dpc) embryos with neuregulin-1, an endocardial-derived growth and differentiation factor essential for ventricular trabeculation, could induce a CCS-like phenotype in embryonic cardiomyocytes (Rentschler et al., 2002). Whereas, the use of in vitro culture systems has demonstrated also that the treatment of embryonic stem cells with endothelin-1 but not with neuregulin-1 increased the percentage of pacemaker-like cells, suggesting that the role of endothelin-1 in CCS development may be conserved, even in mice (Gassanov et al., 2004).

Mesp1 and Mesp2 are transcription factors that contain almost identical basic helix–loop–helix (bHLH) motifs and are encoded by genes that both localize in chromosome 7 (Saga et al., 1996, 1997). Disruption of the *Mesp1* gene results in cardia bifida (Saga, 1998). We also have shown previously, using double knockout mouse embryos and by chimera analysis, that *Mesp1* and *Mesp2* are essential for the development of cardiac mesoderm (Kitajima et al., 2000). *Mesp1* expression is restricted to the nascent mesodermal cells, and its expression is transient and down-regulated before heart tube formation (Saga et al., 1999). However, lineage analysis using *Mesp1-cre* has revealed that *Mesp1*-expressing cells are incorporated into almost all of the precursors of the cardiovascular system (i.e., endothelium, endocardium, myocardium, and epicardium), both in embryonic and extraembryonic regions at 9.5 dpc, and that *Mesp1* expression is the earliest detectable molecular marker in heart precursor cells (Saga et al., 1999, 2000). In this current study, we describe further detailed lineage analyses of the mouse heart using *Mesp1-cre* mice. We show that *Mesp1*-nonexpressing cells contribute to neural crest-derived regions as well as to a subset of the cells in the ventricular CCS.

RESULTS

Lineage Analysis of *Mesp1*-Expressing Mesodermal Cells in the Developing Heart

Using *Mesp1-cre*–mediated cell lineage analysis, we previously reported that *Mesp1*-expressing cells were incorporated into almost all precursors of the cardiovascular system in both embryonic and extraembryonic regions at 9.5 dpc (Saga et al., 2000). However, further analysis at 13.5 dpc now has revealed that the cardiogenic cells are not entirely contributed by *Mesp1*-expressing cells, suggesting that the origin of these cells may be subdivided according to *Mesp1* expression (Fig. 1A–C). At this developmen-

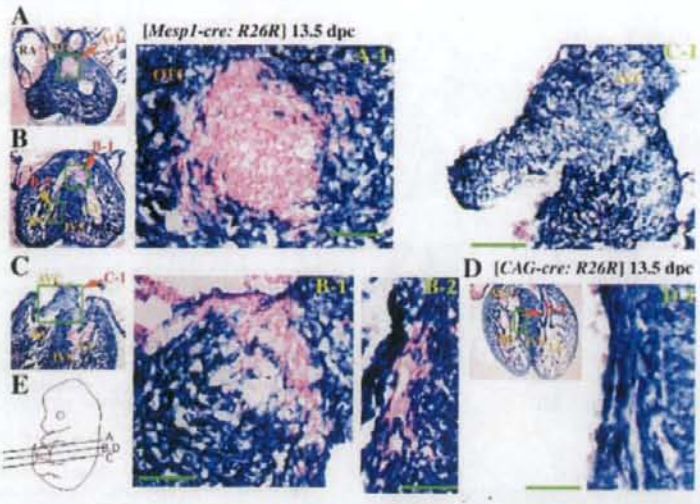

Fig. 1. Transverse sections of β-galactosidase (β-gal) -stained *Mesp1-cre:R26R* or *CAG-cre: R26R* embryos at 13.5 days post coitum (dpc). **A–B:** The β-gal–negative areas were observed in the region of outflow tract cushions (OTC; A; boxed area in A-1) and along the interventricular septum (IVS) in a pattern reminiscent of the ventricular cardiac conduction system (CCS; B; boxed areas, B-1 and B-2). **C:** atrioventricular cushions (AVC; boxed area in C-1) showed β-gal activity. Original magnification, ×100. Magnified images of OT cushion cells, the interventricular regions, and AV cushions are shown in A-1, B-1 and -2, and C-1, respectively. **D:** Transverse sections of β-gal–stained *CAG-cre:R26R* embryos show no β-gal–negative regions, suggesting that *R26R* expression was not shut down as *Mesp1*-nonexpressing cells differentiate. A magnified image in the interventricular regions is shown in D-1. **E:** Sectioning planes are illustrated and were counterstained with eosin. LV, left ventricle; RA, right atrium; RV, right ventricle. Scale bar = 100 μm.

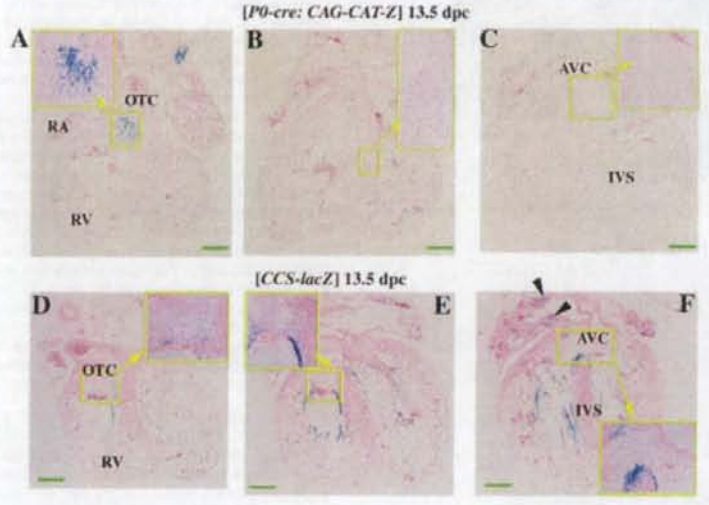

Fig. 2. β-galactosidase (β-gal) staining in sections of the *P0-cre:CAG-CAT-Z* and the *CCS-lacZ* embryos at 13.5 days post coitum (dpc). **A–C:** In the *P0-cre:CAG-CAT-Z* embryo, high β-gal activity is observed in the region of the outflow tract cushion (OTC; A, boxed area), but little activity is evident in the region of the atrioventricular cushion (AVC; C, boxed area). Original magnification, ×40. Note that the β-gal activity was not observed within the ventricle and the interventricular septum (IVS; B). **D–F:** The images in the boxed area are magnified. In the *CCS-lacZ* embryo, β-gal activity is observed strongly in part of the atria (indicated by arrowheads) and along the IVS in a pattern reminiscent of the ventricular cardiac conduction system (CCS; boxed area). In contrast, β-gal activity in either the OTC or AVC regions was barely detectable (D,F). The images in the boxed area are magnified. Sectioning planes of images A–C and D–F are the same as those illustrated in Figure 1E: A–C, respectively. All sections were counterstained with eosin. RA, right atrium; RV, right ventricle. Scale bar = 200 μm.

tal stage (13.5 dpc), during which the septation complexes start to form, *Mesp1*-nonexpressing cells are also visible along the IVS region in a pattern reminiscent of the AVB and bundle branches, which are components of the ventricular CCS (Fig. 1B). In addition, region of the OT cushions had little β-gal activity (Fig. 1A), unlike most of the AV cushions that had strong activity (Fig. 1C). In the *CAG-cre* mouse, in which the *cre* gene is under the control of the cytomegalovirus immediate early enhancer-chicken beta-actin hybrid (*CAG*) enhancer, it has been reported that the sequence between the two *loxP* sites is deleted in all tissues in the mouse embryo (Sakai and Miyazaki, 1997). This finding was confirmed in our current experiments; all of the cells in the developing heart of double-transgenic embryos were positive for *LacZ* (Fig. 1D), indicating that this expression is not down-regulated upon *CAG* promoter activation. This observation strongly suggests that *Mesp1*-"non" expressing cells are indeed present in the developing murine heart of the *Mesp1-cre:R26R* reporter double-transgenic mouse.

Because neural crest cells are known to contribute to part of the developing heart structure (Jiang et al., 2000), we initially expected that the regions containing *Mesp1*-nonexpressing cells might reflect this population. To address this possibility more fully, we next compared our findings with a previous report that used a *P0-cre* transgene and *CAG-CAT-Z* reporter gene to identify neural crest-derived cells (Yamauchi et al, 1999).

Mesp1-Nonexpressing Cells Along the Ventricular Septum Are Not Derived From the Neural Crest

We analyzed *P0-cre:CAG-CAT-Z* embryos to examine whether neural crest cells indeed contribute to any of the regions occupied by *Mesp1*-nonexpressing cells. In the *P0-cre:CAG-CAT-Z* embryo at 13.5 dpc, β-gal activity was mainly detected in the mesenchyme located within the OT cushions of the heart (Fig. 2A), which is consistent with previous findings (Yamauchi et al., 1999) and a report using *Wnt1-cre* mice (Jiang et al.,

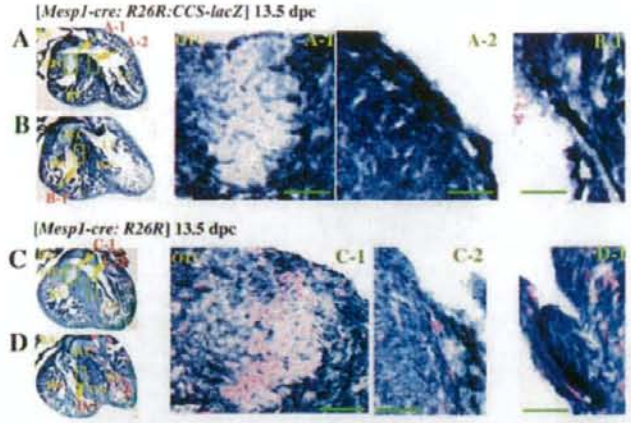

Fig. 3.

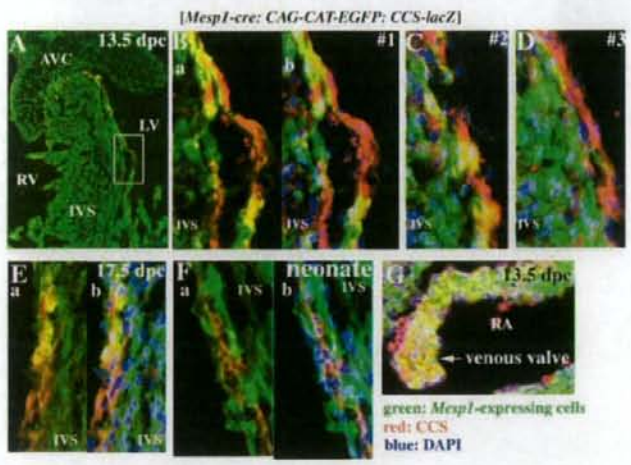

Fig. 4.

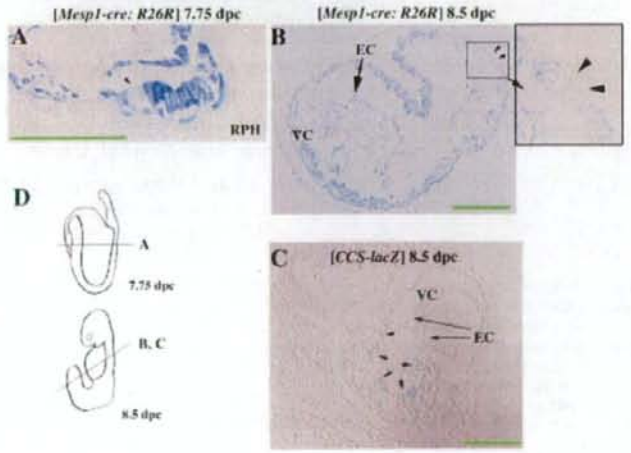

Fig. 5.

Fig. 3. Comparison of β-gal staining patterns between *Mesp1-cre:R26R:CCS-lacZ* triple hetero-embryos and *Mesp1-cre:R26R* embryos. **A,B:** Sections of the heart of the *Mesp1-cre:R26R:CCS-lacZ* embryo at 13.5 days post coitum (dpc). **C,D:** Compared with the *Mesp1-cre:R26R* embryo (boxes in C-2 and D-1), *Mesp1*-nonexpressing cells along the interventricular (IVS) were barely observed in the *Mesp1-cre:R26R:CCS-lacZ* triple hetero-embryos (A,B; boxes in A-2 and B-1). However, *Mesp1*-nonexpressing cells in outflow tract (OT) cushion regions were also detected, even in the triple hetero-embryos (box A-1). Original magnification, ×100. The images in the boxed area are magnified. Sectioning planes of A, B, and C, D are the same as those illustrated in Figure 1E: B and C, respectively. Sections were counterstained with eosin. AVC, atrioventricular cushion; IVS, interventricular septum; RA, right atrium; RV, right ventricle; Scale bar = 100 μm.

Fig. 4. *Mesp1*-nonexpressing cells contribute to a subset of the ventricular cardiac conduction system (CCS). Triple immunostaining for *Mesp1*-expressing cells (green fluorescent protein [GFP] -positive cells; green), cells of the ventricular CCS (LacZ-positive cells; red), and nuclei (4',6'-diamidino-2-phenylindole [DAPI] staining; blue) in a *Mesp1-cre:CAG-CAT-EGFP:CCS-lacZ* embryo. All images shown are merged views, and double immunostaining of GFP and LacZ (a) and a triple immunostaining image with additional DAPI staining (b) are shown in some cases. **A–D:** A merged view of the interventricular (IVS) region at 13.5 days post coitum (dpc). The boxed area of the ventricular CCS in A was magnified as shown in B. Other sections derived from additional embryos are shown in C and D. The presence of red cells suggests that *Mesp1*-nonexpressing cells actually belong to the ventricular CCS, whereas some *Mesp1*-expressing cells also colocalize here (yellow). Typical images of mixed cell populations are shown in B and C, whereas a red cell-dominant section is shown in D. Original magnification, ×400, except for A, which is ×100. **E,F:** Merged view in the IVS region in an embryo at 17.5 dpc (E) or in a neonate (F). Original magnification, ×400. Red cells (i.e., the *Mesp1*-nonexpressing cells belonging to the CCS) were observed even at later stages beyond 13.5 dpc. **G:** The region of the venous valves, which are proposed remnants of the embryonic sinoatrial (SA) ring, at 13.5 dpc. Almost all of the cells in this region were stained yellow, suggesting that the cells belonging to the venous valves are *Mesp1*-expressing. Original magnification, ×200. Sectioning planes are those between B and C, illustrated in Figure 1E. AVC, atrioventricular cushion; LV, left ventricle; OTC, outflow tract cushion; RA, right atrium; RV, right ventricle.

Fig. 5. Comparison of transverse sections of β-gal stained *Mesp1-cre:R26R* embryos with *CCS-lacZ* embryos at an earlier stage. **A:** At 7.75 days post coitum (dpc) in *Mesp1-cre:R26R* embryos, we observed a few *Mesp1*-nonexpressing cells within the primitive heart tube (arrow head). Original magnification, ×400. **B:** At 8.5 dpc, the regions of the *Mesp1*-nonexpressing cells in *Mesp1-cre:R26R* embryos, were observed more clearly (arrowheads). **C:** The β-gal-positive regions (i.e., the cells belonging to the CCS) were observed mainly in the subendocardial myocardium of 8.5 dpc *CCS-lacZ* mouse (arrows). Original magnification, ×200. **D:** Sectioning planes are illustrated. Sections were counterstained with eosin. EC, endocardium; RPH, right primitive heart tube; VC, ventricular chamber. Scale bars = 100 μm.

2000). There were only minimal contributions by neural crest cells in the AV cushions, as predicted by the β-gal activity in the *Mesp1-cre:R26R* mouse (Fig. 2C). Importantly, however, neural crest-derived mesenchyme was not observed in either part of the ventricle or the IVS (Fig. 2B), where *Mesp1*-nonexpressing cells were visible (Fig. 1B). This finding indicates that other cell types must contribute to this particular region. Intriguingly, the distribution of *Mesp1*-nonexpressing cells resembled that of the AVB and bundle branches and also the Purkinje fibers of the CCS. This prompted us to speculate that ventricular CCS cells might be derived from lineages that are distinct from both the neural crest and *Mesp1*-expressing mesodermal cells.

Mesp1-Nonexpressing Cells Contribute to the CCS

As a preliminary approach to determine whether or not *Mesp1*-nonexpressing cells did in fact reside in the CCS, we compared these cells with the β-gal expression patterns in embryonic hearts of *CCS-lacZ* transgenic mice. In these mice, the specialized CCS can be visualized by β-gal activity (Rentschler et al., 2001). In 13.5 dpc hearts from these transgenic animals, strong β-gal activity could be observed in part of the atrium, which could correspond to the SA node. This high level of activity could also be detected along the IVS, which demarcates the ventricular CCS, including the AVB and bundle branches (Fig. 2D–F). When comparing these results with those shown in Figure 1, the portion of the *Mesp1*-nonexpressing cell population along the IVS was found to show a similar pattern to the β-gal–positive regions in the *CCS-lacZ* mice, suggesting that these *Mesp1*-nonexpressing cells contribute to the ventricular CCS.

To provide direct evidence for our hypothesis that cells of the ventricular CCS are indeed derived from *Mesp1*-nonexpressing cells, we generated triple transgenic *Mesp1-cre:R26R:CCS-lacZ* mice. Because both the *CCS-lacZ* and *R26R* transgenic mice use β-gal as a marker, the entire region contributed by the *Mesp1*-nonexpressing cells in the IVS would become β-gal–positive in the triple hetero-embryonic hearts if our contention was correct. As shown in Figure 3, this was found to be the case, as all of the cells in the IVS had β-gal activity, which was in contrast to the corresponding sections of the *Mesp1-cre:R26R* embryo (Fig. 3C,D). Moreover, the region of the OT cushions had little β-gal activity even in the triple hetero-embryo (Fig. 3A), supporting our conclusion that this region is occupied mainly by cells of neural crest origin. Hence, these data suggest that the *Mesp1*-nonexpressing cells in the IVS belong to the ventricular CCS.

It was still unclear, however, whether all of the ventricular CCS is derived from *Mesp1*-nonexpressing cells, because both the *CCS-lacZ* and *R26R* reporter mice use the same β-gal marker. We, therefore, performed a similar series of studies using the *CAG-CAT-EGFP* strain (Kawamoto et al., 2000), in which GFP expression is dependent upon cre-mediated recombination and representative results are shown in Figure 4. *Mesp1*-nonexpressing cells at 13.5 dpc do indeed reside within the ventricular CCS (*Mesp1*-nonexpressing/*CCS-lacZ*-positive red cells in Fig. 4A–D), although it is clear that the CCS is also observed in the *Mesp1*-expressing cell populations (i.e., *Mesp1*-expressing/*CCS-lacZ*–positive yellow cells). In addition, after 4′,6′-diamidino-2-phenylindole (DAPI) staining, we observed that all of the green fluorescent protein (GFP) -negative *Mesp1*-nonexpressing cells belonged to the lacZ-positive cells of the ventricular CCS, because cells positive for DAPI alone (blue) were rarely observed along the IVS (b in Fig. 4A–C). To demonstrate the heterocellular origin of CCS more unequivocally and to analyze the ratios quantitatively, we generated serial sections of the embryonic heart along the anteroposterior axis and analyzed the staining patterns.

A total of three embryos were sectioned and 58 sections containing CCS-LacZ staining in the IVS region were further subjected to semiquantitative analysis (Supplementary Figure S1, which can be viewed at http://www.interscience.wiley.com/jpages/1058-8388/suppmat). However, as the CCS distributes peripherally in the IVS with multiple branchings, it is very difficult to quantify. We, therefore, roughly estimated the ratio by counting DAPI stained nuclei in each cell type and selected 28 typical sections, from which 16 showed a colocalization pattern for yellow and red cells (Fig. 4B,C). Of these 16 sections, 2 and 5 showed a red cell- and a yellow cell-dominant pattern, respectively (Fig. 4D, and data not shown). We have estimated that approximately 20% of the ventricular CCS, along the IVS, corresponds to *Mesp1*-nonexpressing cells. Moreover, red cells (i.e., the *Mesp1*-nonexpressing cells belonging to the ventricular CCS) were also observed in the ventricular CCS even at later developmental stages of 17.5 dpc (Fig. 4E) and in neonates at 4 days after birth (Fig. 4F). The AV cushion cells were weakly positive for the GFP signal, due to the thinness of the cytoplasm and resulting lower intensity of fluorescence (Fig. 4A), but their identity was confirmed by LacZ staining in *Mesp1-cre; R26R* embryos (Fig. 1C). Thus, we conclude unequivocally that the population of *Mesp1*-nonexpressing cells, which we identified along the ventricular septum, contributes to the CCS.

In the case of the SA or AV node regions of the CCS, the contribution of *Mesp1*-expressing and/or *Mesp1*-nonexpressing cells was not as clear from our present results using embryos at 13.5 dpc, because these typical node structures were not discernible. In contrast, we were able to determine that most of the cells in the venous valves, which are the proposed remnants of the embryonic SA ring in the fully developed heart (Rentschler et al., 2001), of the *Mesp1-cre:CAG-CAT-EGFP:CCS-lacZ* embryo were *Mesp1*-expressing (i.e., GFP–positive cells). This determination was revealed by the *Mesp1*-expressing/*CCS-lacZ*–positive yellow cells at 13.5 dpc (Fig. 4G). However, the developmental relationships between the venous valves and both the SA and AV nodes have not yet been determined.

Origin of *Mesp1*-Nonexpressing Cells

To determine the origin of the *Mesp1*-nonexpressing cells, we examined the *LacZ* expression profiles in more immature *Mesp1-cre:R26R* and *CCS-lacZ* embryos. As shown in Figure 5A,

even at 7.75 dpc, at which stage the cardiac crescent can be observed, a few β-gal–negative cells were detectable in the *Mesp1-cre:R26R* embryo. The β-gal–negative cells were observed in the myocardium region more clearly at 8.5 dpc (Fig. 5B). In the *CCS-lacZ* embryo, although the heart region at 7.75 dpc was confirmed to be β-gal–negative (data not shown) as reported previously (Rentschler et al., 2001), patchy staining was observed mainly in the subendocardial myocardium region at 8.5 dpc (Fig. 5C). However, a direct relationship between the *Mesp1*-nonexpressing cells and the CCS cells is still not clear, although the neural crest cells, which are also identifiable as *Mesp1*-nonexpressing cells in our system, have not yet arrived in the heart at this stage and can be excluded (Jiang et al., 2000).

DISCUSSION

In this study, we have found using a Cre-*loxP* site-specific recombination system that the origin of the cardiac mesenchyme is subdivided according to the presence of *Mesp1* expression. We demonstrate that the regions occupied by *Mesp1*-nonexpressing cells correspond to two distinct populations of cells: one derived from the neural crest and the other one that contributes to the ventricular CCS.

Comparison of the Cell-Lineages of Neural Crest Cells and *Mesp1*-Nonexpressing cells

In our experiments with *Mesp1-cre:R26R* embryos, we have found that cells derived from the neural crest are negative but that mesodermal cells derived from *Mesp1*-expressing cells are positive, for β-gal activity. We have also confirmed that mammalian cardiac neural-crest cells are *Mesp1*-negative (Figs. 1, 2) and contribute to the mesenchyme in the OT cushions of the heart. These observations were made following neural crest cell lineage analyses using the *P0-cre:CAG-CAT-Z* strain (Fig. 2) and are consistent with previous results obtained using *Wnt1-cre:R26R* double transgenic mice (Jiang et al., 2000). The origin of the cells of the AV cushions was suggested to be mesodermal, because this region was occupied by *Mesp1*-expressing cells in our study (Fig. 1C). This result is consistent with the previous study of Kisanuki et al. (2001) using *Tie2-cre* mice that reported that the origin of the AV cushions is mainly of endocardial cell lineage. Thus, mesenchymal cells in the OT cushions are derived from mainly neural crest cells and those in the AV cushions are derived from endocardium.

Importantly, we observed a second population of *Mesp1*-nonexpressing cells, along the IVS (Fig. 1B). Because this region is not contributed by neural crest cells (Fig. 2B), we explored the possibility that these *Mesp1*-nonexpressing cells reside in the ventricular CCS. Before examining this possibility, we first confirmed that the failure to express β-gal in the *Mesp1-cre:R26R* embryos was not due to an artifact, such as down-regulation of *LacZ* expression during differentiation or mosaicism of Cre recombinase expression. To exclude the former possibility, we examined *CAG-cre:R26R* mice, in which Cre recombinase is ubiquitously expressed and all cells should be *LacZ*-positive. We did not subsequently observe any *LacZ*-negative cells in the heart, indicating that there had been no down-regulation of *LacZ* upon cell differentiation (Fig. 1D). To exclude possible mosaicism of Cre recombinase, we repeated our analysis in more than 20 embryos and observed very consistent results, although some clonal differences may exist. In addition, when we crossed the *Mesp1-cre* and *CCS-lacZ* strains and monitored *R26R*-dependent reporter gene expression, we did not observe patchy *LacZ*-negative cells in the ventricular wall. Thus, it appears unlikely that mosaicism of the *R26R* reporter could account for our results.

As for the contribution of the neural crest cells into the ventricular CCS, it was reported that neural crest-derived cells were observed in the vicinity of the CCS in the IVS at 14.5 dpc using the *Wnt1-cre:R26R* reporter system (Poelmann et al., 2004). Thus, the possibility cannot be rule out that the neural crest cells contribute to CCS in the IVS, although we could not detect any β-gal–positive cells in the IVS in our *P0-cre:CAG-CAT-Z* system. The discrepancy could be due to the difference in systems used for lineage analyses. The future studies using triple transgenic strategy (*Wnt1-cre:CAG-CAT-GFP:CCS-lacZ*) as used in our current study would be useful to discriminate the discrepancy.

Origins of the CCS

Using *Mesp1-cre:R26R* embryos, we identified a population of *Mesp1*-nonexpressing cells that were found to be distributed in the wall along the ventricular septum (Fig. 1B). The results of genetic crosses with the *CCS-lacZ* strain suggested that these *Mesp1*-nonexpressing cells contribute to the ventricular CCS (Fig. 3B). To confirm these findings, we generated triple transgenic *Mesp1-cre:CAG-CAT-EGFP:CCS-lacZ* mice. Double-staining for GFP and β-gal expression and/or additional DAPI staining in these mice confirmed that the *Mesp1*-nonexpressing cells contribute approximately 20% of the ventricular CCS (Fig. 4). Moreover, these populations of cells can be distinguished at a stage as early as stage 7.75 dpc at least (Fig. 5), whereas *Mesp1* is initially, albeit transiently, expressed at 6.5 dpc (Saga et al., 1996).

The pacemaking and conduction systems of the heart are composed of the SA node, AV node, AVB, the bundle branches, and the Purkinje fibers, each of which can be distinguished morphologically, functionally, and molecularly (Moorman and Christoffels, 2003). The origin of the nodal tissue is less clear than that of the ventricular CCS, although the primary myocardium is suggested to be a candidate (Moorman and Christoffels, 2003). Recently, it was suggested that some of the working myocardium could also differentiate into nodal tissues, even after birth (Pashmforoush et al., 2004). Although the developmental relationships between the venous valves and the nodes have not yet been fully elucidated, our data indicate that most of cells in the venous valves, which are proposed to be remnants of the embryonic SA ring (Rentschler et al., 2001), are derived from *Mesp1*-expressing cells (Fig. 4G). However, further detailed studies will be required to determine the precise cellular origin of the nodes and their relationships with the venous valves.

In the present analyses, we have focused on the cell-lineages of the ventricular CCS and shown them to be of

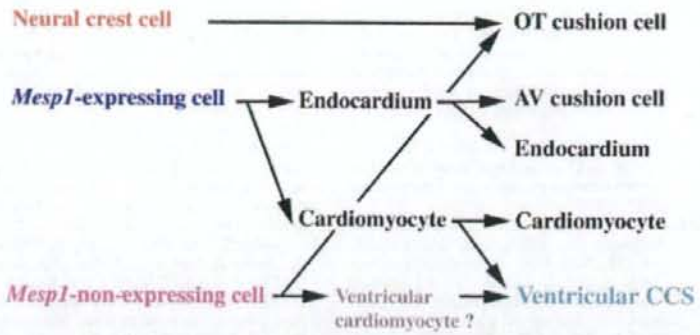

Fig. 6. Summary of the origin and cell-fate relationships of cardiac mesenchyme cell types. Each cardiac cell type is established by three distinct origins: neural crest cells, the mesodermal cells of *Mesp1*-expressing cells, and *Mesp1*-nonexpressing cells. It is noteworthy that both the *Mesp1*-expressing cells and the *Mesp1*-nonexpressing cells contribute to the ventricular CCS. In addition, the origins of the subset of the ventricular CCS that are contributed by the *Mesp1*-nonexpressing cells are distinguishable from that of the myocardium by the *Mesp1* expression profile. We speculate that the *Mesp1*-nonexpressing cardiomyocyte may be a candidate for the origin of the subset of the ventricular CCS. [Color figure can be viewed in the online issue, which is available at www.interscience.wiley.com.]

heterocellular origin. Two possibilities have emerged from both our analyses and previous reports concerning the origin of the ventricular CCS in mouse, occupied by *Mesp1*-nonexpressing cells. First, it is conceivable that the *Mesp1*-nonexpressing cells in the CCS are not derived from cardiomyocytes. Alternatively, these cells may represent cardiomyocytes, which simply do not express *Mesp1*. We favor this latter possibility. Lineage tracing experiments in chick have convincingly demonstrated that the ventricular CCS, including the Purkinje fibers, are derived from cardiomyocytes (reviewed in Mikawa, 1999; Pennisi et al., 2002). Moreover, experiments in the mouse also indicate that embryonic cardiomyocytes can be converted to a CCS-like phenotype in response to neuregulin-1, at least when assayed by up-regulation of the *CCS-lacZ* transgene (Rentschler et al., 2002). Nonetheless, additional analyses will be required to determine the basis for the molecular heterogeneity within the ventricular CCS and to determine whether there is associated functional diversity in this structure.

In conclusion, we have determined that *Mesp1*-nonexpressing cells contribute to the ventricular CCS in addition to the OT cushion. Furthermore, we indicate a possibility that a population of the cells that contribute to the ventricular CCS might be distinguished at an early stage of development. Unfortunately, it could not be clarified from our present experiments whether *Mesp1*-nonexpressing cells also contributed to the other regions of the CCS, such as the SA or AV nodes. A scheme summarizing the cell lineage relationships in the developing murine heart is shown in Figure 6. Our observation that the ventricular CCS includes both *Mesp1*-expressing and -nonexpressing cells is evidence of the heterogeneous nature of the ventricular CCS. The further identification of specific molecular markers for the mouse CCS, expressed at early embryonic stages, will undoubtedly enhance our understanding of the developmental biology of the CCS in the heart.

EXPERIMENTAL PROCEDURES

Lineage Analysis of *Mesp1*-Expressing Cells

The *Mesp1-cre* knockin mouse was constructed by introduction of a gene encoding Cre recombinase into the *Mesp1* locus, as previously described (Saga et al., 1999). The fidelity of expression was confirmed by in situ hybridization at E7.0 (data not shown). Genotyping was performed by polymerase chain reaction using a neo-specific primer NeoAL2: 5′-GGGGATGCGGTGGGCTCTATGGCTT-3′ and *Mesp1* primer MesP1-GR1: 5′-ATATGCCAAGTCATTGAGGTGAGCTTTC-3′. *Mesp1-cre* mice were crossed with either *CAG-CAT-Z* (Araki et al., 1995), *R26R* (Soriano, 1999), or *CAG-CAT-EGFP* (Kawamoto et al., 2000) reporter mice. *P0-cre* (Yamauchi et al., 1999) and *CCS-lacZ* mice (Rentschler et al., 2001) were also used for cell lineage analyses. Mice were maintained on a 7:00 AM to 7:00 PM light–dark cycle, with noon on the day of vaginal plug discovery defined as 0.5 dpc.

β-gal Staining, Immunostaining, and In Situ Hybridization

Embryos that had been fixed at 7.5–10.5 dpc were stained for the detection of β-galactosidase activity in whole-mounts as described previously (Saga et al., 1992). The specimens were then dehydrated by means of a graded ethanol series, embedded in either paraffin wax or plastic resin (technovit 8100, Heraeus Kulzer, Inc.) and sectioned at a thickness of 4 μm. Hearts that had been isolated from embryos at later stages were subjected to β-gal staining after sectioning. Briefly, hearts were fixed in a solution of 2% paraformaldehyde, 0.05% glutaraldehyde, and 0.02% NP-40 in phosphate buffer (PBS) for 30 min on ice. The tissues were then sequentially soaked in a graded series of 10, 20, and 30% sucrose (w/v) in PBS while being gently agitated on a shaking platform, culminating in a 50:50 mix of 30% sucrose:OCT. Samples were frozen and stored at −80°C until sectioning at 8 μm thickness, and the sections were placed on gelatin-coated slides. Frozen sections of *Mesp1-cre:CAG-CAT-EGFP:CCS-lacZ* mouse hearts was stained with anti-lacZ and anti-GFP antibodies as follows: sections prepared were fixed with 4% paraformaldehyde for 3 min, treated with 10 μg/ml proteinase K and blocked in 3% skim milk for 30 min at room temperature (RT). Blocking solutions was replaced with rabbit anti-β-gal antibody (Cappel, ICN Pharmaceuticals, Inc., OH) at a dilution of 1:2,000 and with rat anti-GFP antibody (Nacalai Tesque, Kyoto, Japan) at a dilution 1:200 and incubated overnight at 4°C. After brief washes in PBS, the sections were incubated with Alexa 594–conjugated anti-rabbit followed by Alexa 488–conjugated anti-rat secondary antibodies at dilutions of 1:200

for 90 min at RT. These sections were then incubated with 0.1 μg/ml of DAPI (Sigma, St. Louis, MO) for 5 min to visualize nuclei.

ACKNOWLEDGMENTS

We thank the following researchers for providing mice: Dr. Jun-ichi Miyazaki (*CAG-cre*, *CAG-CAT-Z*, and *CAG-CAT-EGFP*), Dr. Kuniya Abe (*P0-cre*), Dr. Philippe Soriano (*R26R*), and Dr. Glenn I. Fishman (*CCS-lacZ*). We also thank Seiko Shinzawa, Mariko Ikumi, Eriko Ikeno, Chizuko Obata, Shinobu Watanabe, and Maho Endo for technical assistance.

REFERENCES

Araki K, Araki M, Miyazaki J, Vassalli P. 1995. Site specific recombination of a transgene in fertilized eggs by transient expression of Cre recombinase. Proc Natl Acad Sci U S A 92:160–164.

Cheng G, Litchenberg WH, Cole GJ, Mikawa T, Thompson RP, Gourdie RG. 1999. Development of the cardiac conduction system involves recruitment within a multipotent cardiomyogenic lineage. Development 126:5041–5049.

Coppen SR, Dupont E, Rothery S, Severs NJ. 1998. Connexin45 expression is preferentially associated with the ventricular conduction system in mouse and rat heart. Circ Res 82:232–243.

Coppen SR, Severs NJ, Gourdie RG. 1999. Connexin45 (alpha 6) expression delineates an extended conduction system in the embryonic and mature rodent heart. Dev Genet 24:82–90.

Delorme B, Dahl E, Jarry-Guichard T, Marics I, Briand JP, Willecke K, Gros D, Theveniau-Ruissy M. 1995. Developmental regulation of connexin 40 gene expression in mouse heart correlates with the differentiation of the conduction system. Dev Dyn 204:358–371.

Gassanov N, Er F, Zagidullin N, Hoppe UC. 2004. Endothelin induces differentiation of ANP-EGFP expressing embryonic stem cells towards a pacemaker phenotype. FASEB J 18:1710–1712.

Gourdie RG, Mima T, Thompson RP, Mikawa T. 1995. Terminal diversification of the myocyte lineage generates Purkinje fibers of the cardiac conduction system. Development 121:1423–1431.

Jiang X, Rowitch DH, Soriano P, McMahon AP, Sucov HM. 2000. Fate of the mammalian cardiac neural crest. Development 127:1607–1616.

Kawamoto S, Niwa H, Tashiro F, Sano S, Kondoh G, Takeda J, Tabayashi K, Miyazaki J. 2000. A novel reporter mouse strain that expresses enhanced green fluorescent protein upon Cre-mediated recombination. FEBS Lett 470: 263–268.

Kirby ML, Gale TF, Stewart DE. 1983. Neural crest cells contribute to normal aorticopulmonary septation. Science 220: 1059–1061.

Kisanuki YY, Hammer RE, Miyazaki J, Williams SC, Richardson JA, Yanagisawa M. 2001. Tie2-Cre transgenic mice: a new model for endothelial cell-lineage analysis in vivo. Dev Biol 230:230–242.

Kitajima S, Takagi A, Inoue T, Saga Y. 2000. MesP1 and MesP2 are essential for the development of cardiac mesoderm. Development 127:3215–3226.

Kupershmidt S, Yang T, Anderson ME, Wessels A, Niswender KD, Magnuson MA, Roden DM. 1999. Replacement by homologous recombination of the minK gene with lacZ reveals restriction of minK expression to the mouse cardiac conduction system. Circ Res 84:146–152.

Mikawa T. 1999. Cardiac lineages. In: Harvey RP, Rosenthal N, editors. Heart development. San Diego: Academic Press. p 19–33.

Moorman AFM, Christoffels VM. 2003. Cardiac chamber formation: development, genes, and evolution. Physiol Rev 83:1223–1267.

Moorman AFM, deJong F, Denyn MM, Lamers WH. 1998. Development of the cardiac conduction system. Circ Res 82: 629–644.

Myers DC, Fishman GI. 2004. Toward an understanding of the genetics of murine cardiac pacemaking and conduction system development. Anat Rec A Discov Mol Cell Evol Biol 280:1018–1021.

Nguyen-Tran VT, Kubalak SW, Minamisawa S, Fiset C, Wollert KC, Brown AB, Ruiz-Lozano P, Barrere-Lemaire S, Kondo R, Norman LW, et al. 2000. A novel genetic pathway for sudden cardiac death via defects in the transition between ventricular and conduction system cell lineages. Cell 102:671–682.

Pashmforoush M, Lu JT, Chen H, Amand TS, Kondo R, Pradervand S, Evans SM, Clark B, Feramisco JR, Giles W, Ho SY, Benson DW, Silberbach M, Shou W, Chien KR. 2004. Nkx2–5 pathways and congenital heart disease; loss of ventricular myocyte lineage specification leads to progressive cardiomyopathy and complete heart block. Cell 117:373–386.

Pennisi DJ, Rentschler S, Gourdie RG, Fishman GI, Mikawa T. 2002. Induction and patterning of the cardiac conduction system. Int J Dev Biol 46:765–775.

Poelmann RE, Jongbloed MR, Molin DG, Fekkes ML, Wang Z, Fishman GI, Doetschman T, Azhar M, Gittenberger-de Groot AC. 2004. The neural crest is contiguous with the cardiac conduction system in the mouse embryo: a role in induction? Anat Embryol (Berl) 208:389–393.

Rentschler S, Vaidya DM, Tamaddon H, Degenhardt K, Sassoon D, Morley GE, Jalife J, Fishman GI. 2001. Visualization and functional characterization of the developing murine cardiac conduction system. Development 128:1785–1792.

Rentschler S, Zander J, Meyers K, France D, Levine R, Porter G, Rivkees SA, Morley GE, Fishman GI. 2002. Neuregulin-1 promotes formation of the murine cardiac conduction system. Proc Natl Acad Sci U S A 99:10464–10469.

Saga Y. 1998. Genetic rescue of segmentation defect in MesP2-deficient mice by MesP1 gene replacement. Mech Dev 75: 53–66.

Saga Y, Yagi T, Ikawa Y, Sakakura T, Aizawa S. 1992. Mice develop normally without tenascin. Genes Dev 6:1821–1831.

Saga Y, Hata N, Kobayashi S, Magnuson T, Seldin M, Taketo MM. 1996. MesP1: a novel basic helix-loop-helix protein expressed in the nascent mesodermal cells during mouse gastrulation. Development 122:2769–2778.

Saga Y, Hata N, Koseki H, Taketo MM. 1997. Mesp2: a novel mouse gene expressed in the presegmented mesoderm and essential for segmentation initiation. Genes Dev 11:1827–1839.

Saga Y, Miyagawa-Tomita S, Takagi A, Kitajima S, Miyazaki J, Inoue T. 1999. MesP1 is expressed in the heart precursor cells and required for the formation of a single heart tube. Development 126: 3437–3447.

Saga Y, Kitajima S, Miyagawa-Tomita S. 2000. *Mesp1* expression is the earliest sign of cardiovascular development. Trends Cardiovasc Med 10:345–352.

Sakai K, Miyazaki J. 1997. A transgenic mouse line that retains Cre recombinase activity in mature oocytes irrespective of the cre transgene transmission. Biochem Biophys Res Commun 237:318–324.

Soriano P. 1999. Generalized lacZ expression with the ROSA26 Cre reporter strain. Nat Genet 21:70–71.

Waldo K, Miyagawa-Tomita S, Kumiski D, Kirby ML. 1998. Cardiac neural crest cells provide new insight into septation of the cardiac outflow tract: aortic sac to ventricular septal closure. Dev Biol 196: 129–144.

Yamauchi Y, Abe K, Mantani A, Hitoshi Y, Suzuki M, Osuzu F, Kuratani S, Yamamura K. 1999. A novel transgenic technique that allows specific marking of the neural crest cell lineage in mice. Dev Biol 212:191–203.

Available online at www.sciencedirect.com
SCIENCE DIRECT
Biochemical and Biophysical Research Communications 342 (2006) 766–772
BBRC
www.elsevier.com/locate/ybbrc

Periostin is an extracellular matrix protein required for eruption of incisors in mice

Isao Kii [a], Norio Amizuka [b], Li Minqi [b], Satoshi Kitajima [c], Yumiko Saga [d], Akira Kudo [a,*]

[a] Department of Biological Information, Tokyo Institute of Technology, Yokohama 226-8501, Japan
[b] Center for Transdisciplinary Research, Niigata University, Niigata 951-8514, Japan
[c] Division of Cellular and Molecular Toxicology, National Institute of Health Science, Tokyo 158-8501, Japan
[d] Division of Mammalian Development, National Institute of Genetics, Mishima 411-8540, Japan

Received 27 January 2006
Available online 14 February 2006

Abstract

A characteristic tooth of rodents, the incisor continuously grows throughout life by the constant formation of dentin and enamel. Continuous eruption of the incisor is accompanied with formation of shear zone, in which the periodontal ligament is remodeled. Although the shear zone plays a role in the remodeling, its molecular biological aspect is barely understood. Here, we show that periostin is essential for formation of the shear zone. *Periostin*$^{-/-}$ mice showed an eruption disturbance of incisors. Histological observation revealed that deletion of *periostin* led to disappearance of the shear zone. Electron microscopy revealed that the disappearance of the shear zone resulted from a failure in digestion of collagen fibers in the *periostin*$^{-/-}$ mice. Furthermore, immunohistochemical analysis using anti-periostin antibodies demonstrated the restricted localization of periostin protein in the shear zone. Periostin is an extracellular matrix protein, and immunoelectron microscopy showed a close association of periostin with collagen fibrils in vivo. These results suggest that periostin functions in the remodeling of collagen matrix in the shear zone.

Keywords: Periostin; Incisor; Collagen; Eruption; Periodontal ligament; Shear zone; Tooth; Fasciclin

The periodontal ligament is a dense connective tissue containing fibroblastic cells and vascular and neural elements [1,2]. Thick collagen bundles, i.e., principal periodontal fibers, run between the cementum and alveolar bone, and some of them penetrate into these tissues as Sharpey's fibers. The periodontal ligament serves as a cushion as well as an anchor between the teeth and the alveolar bone during mastication. Tooth eruption and orthodontic tooth movement induce the active remodeling of the periodontal ligament, following to realignment of teeth. Several MMPs are reported to be involved in the remodeling of the periodontal ligament [3–7].

Rodent's incisors, having a sharp chisel-like shape, differ from other teeth, molars, in certain biological properties: incisors erupt continuously throughout life. The labial portion of these teeth is covered with enamel, and the remaining surface with cementum. Previously, it was reported that the periodontal ligament of the rodent incisor comprises two compartments: a highly vascularized part and an unvascularized part, and these are also called the alveolus-related part and the tooth-related part, respectively [8]. The former, which localizes closer to the alveolar bone, is regarded as the non-moving zone, whereas the latter is the zone that moves during continuous incisor eruption. The boundary between these alveolus- and tooth-related parts is referred to as the shear zone [8]. Synthesis and turnover of total proteins occur throughout the periodontal ligament, whereas remodeling of collagens predominantly occurs in the shear zone [9]. Although the shear zone plays an important role in the remodeling of the periodontal ligament, its molecular biological aspect is barely understood.

* Corresponding author. Fax: +81 45 924 5718.
E-mail address: akudo@bio.titech.ac.jp (A. Kudo).

0006-291X/$ - see front matter © 2006 Elsevier Inc. All rights reserved.
doi:10.1016/j.bbrc.2006.02.016

In the previous studies, we succeeded in identifying an extracellular matrix protein that we termed periostin because of its specific expression patterns in the periosteum and periodontal ligament in adult mice [10–12]. In addition, observations on the fetal mouse demonstrated the expression of periostin in the fascias of muscles, perichondrium, articular surfaces of the epiphyseal cartilage, and joint ligaments [13,14]. Thus, periostin expression is temporally regulated and spatially restricted mostly to the cells of connective tissues, suggesting its potential role in the formation and maintenance of the tendinous connective tissue structures.

In this study, we found that *periostin*$^{-/-}$ mice showed an eruption disturbance of incisors and intended to obtain a mechanistic insight into how the shear zone was maintained in the continuous eruption of incisors.

Materials and methods

Animals. The *periostin*$^{-/-}$ mouse was generated in our laboratory (Kii et al. [15] and Shimazaki et al., manuscript in preparation). Simply, we performed targeted disruption of the periostin gene in mouse embryonic stem (ES) cells using homologous recombination, and the inserted Neo gene was finally deleted in deficient mice by crossing with CAG-Cre mice to excise the neo cassette, and no periostin expression was observed. The *periostin*$^{-/-}$ mice were viable, and the newborns appeared normal. All animals were allowed free access to standard mouse chow and water during the whole experimental period.

Histological analysis. We used four 6-week-old male mice and six 12-week-old male mice homozygous for the disrupted *periostin* gene, and the same number of their wild-type littermates. The mice were perfused through the left ventricle with 4% paraformaldehyde in 0.1 M phosphate buffer (pH 7.4). The mandibles were removed and immersed in the same fixative for an additional 12 h and then decalcified with EDTA solution for 3 weeks. Paraffin sections were prepared and incubated with an antiserum against mouse periostin. Final visualization of immuno-reaction sites was accomplished with 3-3′ diaminobenzidine. Rabbit anti-periostin antibodies were previously described [12].

Immunoelectron microscopy. Cryostat sections obtained from fixed and decalcified specimens were incubated with rabbit polyclonal antisera against mouse periostin and subsequently with HRP-conjugated secondary antibody. The immuno-reactions were visualized with 3-3′ diaminobenzidine. For immunoelectron microscopy, the specimens were processed as described previously [16].

Eruption experiment. To determine if *periostin* would be physiologically involved in the eruption of the incisors, we cut off one of the two lower incisors in the wild-type and the *periostin*$^{-/-}$ mice at the gingival margin. The erupted incisors were then observed 4 days post-operation.

Results

Eruption disturbance of incisors in the periostin$^{-/-}$ *mice*

The *periostin*$^{-/-}$ mice were viable, and the newborns appeared normal. However, as early as 6 weeks after birth, the incisors from the *periostin*$^{-/-}$ mice were shorter than those from the wild-type littermates (data not shown). In 12-week-old wild-type mice, their incisors were nearly adjoined, with only a narrow space between them (Fig. 1A). In contrast, in the 12-week-old *periostin*$^{-/-}$ mice, lower incisors were shorter than those in the wild-type littermates, and the space between the incisors was wider (Fig. 1B), furthermore, they displayed a chalky white color,

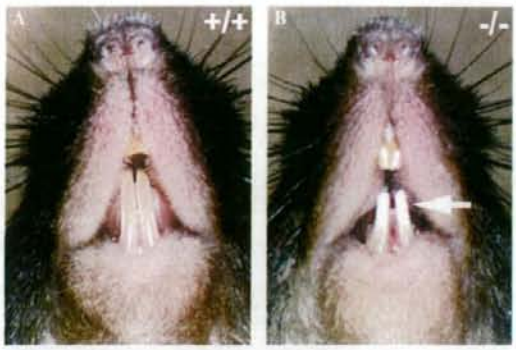

Fig. 1. Abnormal appearance of incisors in the *periostin*$^{-/-}$ mice. Photographs of incisors in 12-week-old wild-type (A) and *periostin*$^{-/-}$ (B) mice. The arrow in (B) indicates short and chalky white incisors in this *periostin*$^{-/-}$ mouse.

indicating disorganization of the enamel layers (Fig. 1B, arrow). Upper incisors of the 12-week-old *periostin*$^{-/-}$ mice also showed similar abnormal phenotypes.

To further investigate whether *periostin* is physiologically involved in eruption of incisors, we cut off one of two lower incisors in the 12-week-old wild-type and the *periostin*$^{-/-}$ mice at the gingival margin, and observed the eruption of incisors 4 days post-operation. In the *periostin*$^{-/-}$ mice, the eruption of the incisor was severely disrupted (Fig. 2B), while in the wild-type mice it normally occurred

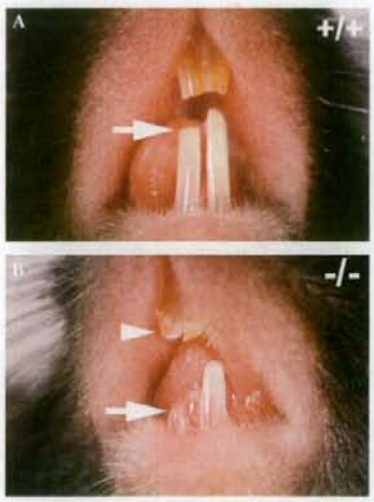

Fig. 2. Eruption disturbance of incisors in the *periostin*$^{-/-}$ mice. Photographs showing incisors that erupted 4-days post-amputation in 12-week-old wild-type (A) and *periostin*$^{-/-}$ (B) mice. In the wild-type mouse, the amputated incisor (left) erupted to the same degree as the intact incisor (right); whereas in the *periostin*$^{-/-}$ animal, the amputated incisor (left) barely erupted. Arrows indicate top of the amputated incisors. Abnormal teeth in the *periostin*$^{-/-}$ mouse are also noted (arrowhead).

(Fig. 2A). These results indicate that periostin acts on the eruption of the incisors.

Disorganization of enamel and dentin layers in the periostin$^{-/-}$ incisors

To investigate the tissue formation in the *periostin*$^{-/-}$ incisors, we performed the histological analyses at the apical region of the incisors. The incisors of rodents are permanently built from the apical bud, and are pushed out anteriorly. In the histological analysis of the apical region in the 6-week-old *periostin*$^{-/-}$ mice, the obvious focal disorganization of ameloblastic layers and the thick dentin and enamel layers, which were waved gently, were observed (Fig. 3B, arrow), compared with those tissues in the wild-type mice (Fig. 3A), although in the *periostin*$^{-/-}$ mice the apical bud generating dental pulp, dentin, and enamel was observed. In the 12-week-old *periostin*$^{-/-}$ mice, the incisal enamel and dentin layers were compressed and undulated (Fig. 3D), though in the wild-type mice they were thin and smooth (Fig. 3C). These findings imply that the incisors in the *periostin*$^{-/-}$ mice became more compressed and undulated from 6- to 12-week-old mice.

In rodents, tooth development, enamel covering of tooth is built in four distinct steps. The first step is the secretion of extracellular matrices and the initiation of enamel crystal growth by polarized ameloblasts (the secretory stage). The second step is the matrix degradation and the differentiation of ameloblasts (the transition stage). The third step is the removal of residual protein components and the crystal growth (the maturation stage). The fourth step is the complete of covering with enamel (the mature stage). These enamel formation processes are found on each incisor of adult mice from the apical region to the front orderly, because of the continuous enamel formation due to the growth and eruption of incisors. High magnification of the ameloblastic layer of the 12-week-old wild-type mice showed a dense cell layer consisting of polarized ameloblasts (nuclei located proximally) in the secretory stage (Fig. 3E), and ameloblasts in the maturation stage (Fig. 3G). In the 12-week-old *periostin*$^{-/-}$ mice, this cell layer was loosened, and partial non-polarized ameloblasts were observed in the secretory stage (Fig. 3F). Moreover, the gaps between the polarized ameloblasts appeared in the maturation stage (Fig. 3H). These histological observations demonstrated that in the *periostin*$^{-/-}$ mice, the morphology and alignment of the ameloblasts were severely disrupted, indicating the impaired enamel layer formation in the absence of *periostin* gene.

The shear zone in the periostin$^{-/-}$ mice

Furthermore, we examined the immunohistological localization of periostin protein at the apical region of the incisors in the 12-week-old wild-type mice. A positive immunoreaction for periostin was observed only in the periodontal ligament of incisors (Fig. 4). At a high magnification, the strong immuno-reactivity for periostin was observed in the middle region of the periodontal ligament corresponding to the shear zone that is the boundary between tooth- and alveolus-related parts (Fig. 4C, arrows), whereas a faint staining was observed in the periodontal ligament close to the cementum and the alveolar bone surface (Fig. 4C). Thus, this strong immuno-reactivity for periostin in the shear zone indicates a role for periostin protein in the shear zone for eruption of the incisors.

To address the requirement for periostin protein in the shear zone, we histologically analyzed sections of the periodontal ligament around the incisors in the *periostin*$^{-/-}$ mice. The shear zone was clearly distinguishable

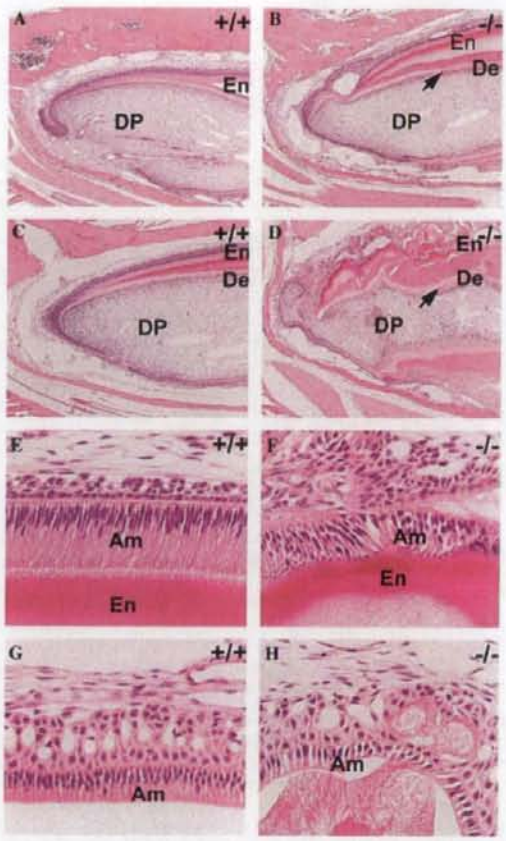

Fig. 3. Histological analysis of the apical region of incisors in the *periostin*$^{-/-}$ mice. Representative histological sections (hematoxylin/eosin stain) of the apical region (root) of incisors in the mandibles from 6-week- (A,B) and 12-week- (C,D) old wild-type (+/+) and *periostin*$^{-/-}$ (−/−) mice show that incisal enamel and dentin are compressed and undulated in the *periostin*$^{-/-}$ mice (arrows). Histological sections (hematoxylin/eosin staining) at high magnifications of the secretory stage (E,F) and the maturation stage (G,H) of enamel in 12-week-old wild-type (+/+) and *periostin*$^{-/-}$ (−/−) mice show disorganized enamel layers in the *periostin*$^{-/-}$ mice. DP, dental pulp; En, enamel; De, dentin; Am, ameloblastic layer.

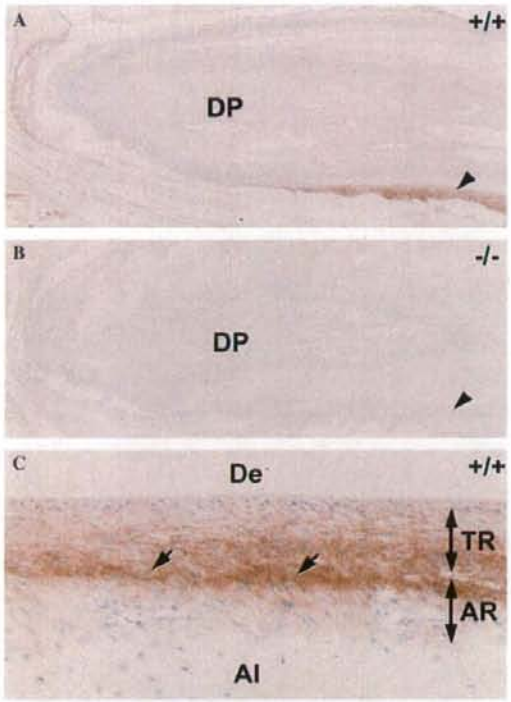

Fig. 4. Immunohistological localization of periostin protein in the periodontal ligament. Immuno-localization of periostin in the periodontal ligament of incisors (A,C) from 12-week-old wild-type (A,C) and *periostin*$^{-/-}$ (B) mice. The specific immunoreactivity for periostin is seen in the wild-type periodontal ligament (A, arrowhead), whereas *periostin*$^{-/-}$ mice have no expression of periostin protein there at all (B, arrowhead). Arrows in (C) indicate the shear zone, which is the boundary between the TR (tooth-related) and AR (alveolus-related) regions. Strong immunoreactivity for periostin is observed in the shear zone of the incisor periodontal ligament. DP, dental pulp; De, dentin; Al, alveolar bone.

in hematoxylin and eosin-stained sections from both the control 6- and the 12-week-old wild-type mice, and it appeared as a line when observed by microscopy (Figs. 5A and C, arrows). In the 6-week-old *periostin*$^{-/-}$ mice, the line in the shear zone was obscure (Fig. 5B). Notably, in the 12-week-old *periostin*$^{-/-}$ mice, the shear zone was completely disappeared, and the periodontal ligament was wider than that of the wild-type mice (Fig. 5D).

To examine the ultrastructure of the shear zone in the *periostin*$^{-/-}$ mice, we carried out electron-microscopic examination of the periodontal ligament around the incisors. In the 12-week-old wild-type mice, we observed the presence of fragmented collagen fibrils extracellularly (Fig. 5E), suggesting digestion of collagen fibrils in the shear zone. In contrast, in the *periostin*$^{-/-}$ mice, abundant intact collagen fibrils occupied the shear zone, and the line disappeared (Fig. 5F). These results suggest that *periostin* is required for the digestion process of collagen fibrils in the shear zone.

Periostin protein localized to collagen fibrils

To understand the molecular mechanism leading to formation of the shear zone, we focused on the extracellular matrix localization of periostin protein, because periostin is known to be localized in the boundary between the cells and extracellular matrix [12–14].

To investigate the extracellular matrix localization of periostin in the periodontal ligament in vivo, we conducted immuno-electron microscopic analysis using anti-periostin antibodies. Our results showed that the immuno-reactivity was detected mainly on the extracellular collagen fibrils, suggesting a possible interaction between periostin protein and collagen fibrils (Figs. 6A and B).

Discussion

In this study based on observations on *periostin*$^{-/-}$ mice, we show that *periostin* is required for formation of the shear zone in the periodontal ligament of incisors. Although several MMPs are involved in remodeling of the periodontal ligament in the previous studies [3–7], the molecular biological aspect of the shear zone is not studied well. The present study showed that periostin protein localized to the shear zone and interacted to the collagen fibrils. Since it was reported that remodeling of collagens predominantly occurs in the shear zone [9], our findings suggest that periostin protein plays a role in remodeling of collagen matrix.

Our electron microscopic analysis in the wild-type mice demonstrated that the digestion of collagen fibers occurred in the shear zone, suggesting that digestion of collagen fibers in this zone may be necessary for an appropriate eruption of incisors. However, in the *periostin*$^{-/-}$ mice, the same observation showed existence of abundant collagen fibers in the intercellular spaces and few digested ones compared with the wild-type littermates. The collagen fibers detected in the periodontal ligament of the *periostin*$^{-/-}$ mice appeared to connect the cementum to the alveolar bone tightly. This tight connection may have prevented the eruption of incisors in the *periostin*$^{-/-}$ mice.

In the *periostin*$^{-/-}$ mice, the defective remodeling in the periodontal ligament of the incisors became more severe as the animals aged. This observation indicates that no remodeled and metabolized extracellular matrices are accumulated to form an abnormal ligament as the animals aged in the absence of *periostin*.

Because disruption of the *periostin* gene caused the accumulation of undigested collagen fibers, periostin may be connected with the digestion of collagen fibers in the shear zone. In the shear zone, the movement between the tooth- and alveolus-related parts causes mechanical stress, and periodontal fibroblasts must sense and respond to this stress. In previous reports, expression of periostin was increased under the mechanically stressful condition of orthodontic tooth movement [17], and decreased by occlusal hypofunction in the mouse periodontal ligament [18].

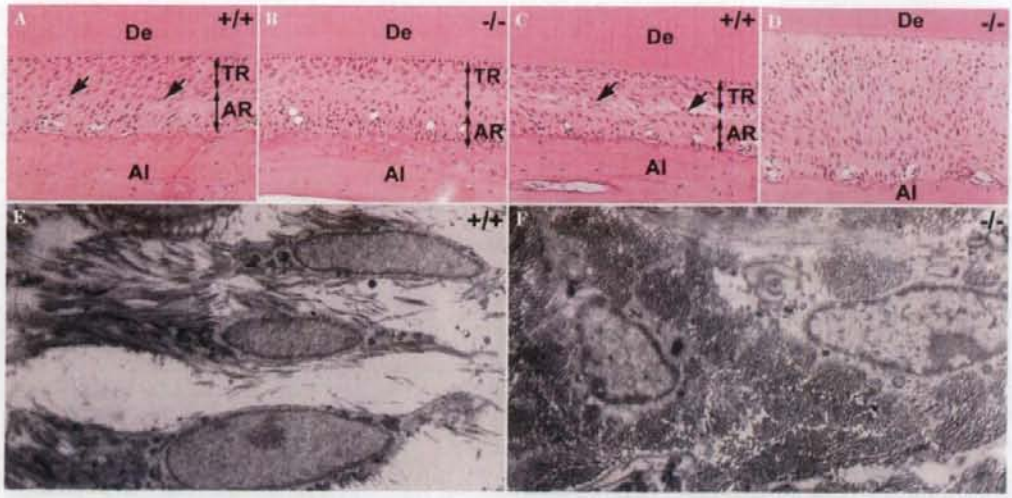

Fig. 5. Remodeling of the periodontal ligament of incisors is defective in periostin$^{-/-}$ mice. Histological micrographs (hematoxylin/eosin staining) of the periodontal ligament from 6-week- (A,B) and 12-week- (C,D) old wild-type (+/+) and periostin$^{-/-}$ (−/−) mice. Arrows indicate the shear zone, which is the boundary between the TR (tooth-related) and AR (alveolus-related) regions. The shear zone in wild-type mice (A,C) is clearly distinguishable, whereas it is obscure in 6-week-old periostin$^{-/-}$ mice (B) and is completely absent in 12-week-old periostin$^{-/-}$ mice (D). Electron microscopy of the incisor periodontal ligament shows evidence of digestion of collagen fibers in 12-week-old wild-type mice (E), but undigested and abundant collagen bundles in 12-week-old periostin$^{-/-}$ mice (F). DP, dental pulp; En, enamel; De, dentin; Al, alveolar bone; TR, tooth-related region; and AR, alveolus-related region.

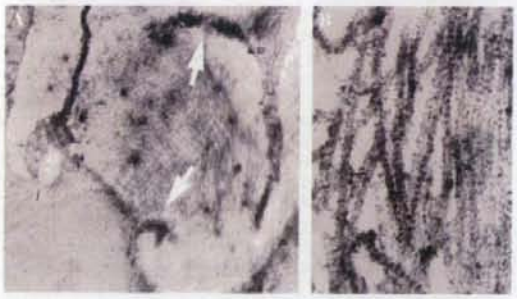

Fig. 6. Immuno-electron microscopic analysis for periostin. Immunoreactivity for periostin is observed in the boundary between cells and the extracellular matrix in the periodontal ligament of the wild-type mice (A, arrows). At a high magnification of the collagen fibers, periostin is seen to be associated with the collagen fibers (B).

These results indicate that in the shear zone, mechanical stress caused by the movement of tooth-related parts may increase the expression of periostin in the shear zone.

The *periostin*$^{-/-}$ mice showed abnormal appearance of incisors, especially disorganized enamel layers and compressed and undulated dentin layers. The present study demonstrates the specific function of periostin in the shear zone. We concluded that the incisors of the *periostin*$^{-/-}$ mice were continuously built in the apical region, but could not erupt because of the defective remodeling of the periodontal ligament, therefore, demonstrating the compressed appearance of the enamel and dentin of their incisors.

However, there is one question whether *periostin* is involved in formation of the enamel and dentin, and affects the functions of the ameloblast and odontoblast directly. In the ameloblastic layer and the apical bud, expression of periostin is barely observed. Periostin localized to the periodontal ligament specifically in the incisors of mice, suggesting that the function of periostin may be restricted to the periodontal ligament.

Our recent findings indicate that periostin protein binds directly to type I collagen in vitro (Shimazaki et al., manuscript in preparation). Periostin protein in the periodontal ligament was associated with the collagen fibers in vivo. These results suggest that periostin protein in vivo binds to type I collagen fibers directly. Periostin is a member of the fasciclin I family, whose members include β ig-h3 protein [10]. It has been reported that β ig-h3 also binds to collagens directly [19,20]. Our results and these previous reports suggest a common function between periostin and β ig-h3 proteins. Furthermore, periostin acts as a cell spreading factor for fibroblastic cells [12,21] and is reported as a ligand for integrin αVβ3 or αVβ5 [21–23], and its four Fas I domains are postulated to be a binding domain for integrin from the results of biochemical analysis of β ig-h3 [24,25]. These findings imply the existence of a collagen–periostin–integrin complex in the shear zone.

Periostin is a highly conserved protein among various species such as human, dog, rat, mouse, chick, and zebrafish (data not shown). Zebrafish periostin is required for formation of the myoseptum, which is composed of dense collagens [26]. The myoseptum is a connective tissue

layer that divides the somites from the trunk [27]. The structure and function of the myoseptum are similar to those of the mammalian tendon. Both the myoseptum and tendon serve as the transmitter of muscular contractility to bones and adjoining muscles, and their structures are indispensable for movement of vertebrate animals. The tendon is also composed of dense collagen fibers, and is exposed to mechanical stress caused by physical exercise, just as are the periodontal ligament and the periosteum [28,29]. Furthermore, expression of mouse periostin is also found in tendons [13]. Tissues that are exposed to strong mechanical stress form a dense collagenous extracellular matrix, and this matrix is remodeled sufficiently to tolerate the stress when the tissues are deformed by strong mechanical stress beyond the permissible range. These previous findings and our present results suggest that periostin is responsible for triggering the remodeling of collagenous tissues.

To our knowledge, this is the first report on a molecule responsible for formation of the shear zone. The periodontal ligament in humans is also responsible for the eruption and realignment of teeth. The *periostin* is a gene whose sequence is highly conserved between mice and humans [10], and periostin protein was also detected in the human periodontal ligament (unpublished results). Therefore, *periostin*$^{-/-}$ mice provide a novel model system to evaluate the cause of eruption disturbance and malocclusion in humans.

Acknowledgments

We thank A. Moriyama, Y. Nakatani, and M. Shimazaki for critical reading of the manuscript; E. Ikeno for technical assistance in the generation of *periostin*$^{-/-}$ mice; Y. Hattori for technical assistance in protein purification; M. Ikumi, T. Nishiyama, Y. Nagano, and K. Kume for the maintenance and manipulation of the animals; H. Tanabe, A. Oshima, and K. Horiuchi for their technical advice. This work was supported by grants from the Promotion of Niigata University Research Project and from the Ministry of Education, Sports, Science and Technology.

References

[1] P. Lekic, J. Rojas, C. Birek, H. Tenenbaum, C.A. McCulloch, Phenotypic comparison of periodontal ligament cells in vivo and in vitro, J. Periodontal Res. 36 (2001) 71–79.

[2] B.K. Berkovitz, Periodontal ligament: structural and clinical correlates, Dent. Update 31 (2004) 46–50, pp. 52, 54.

[3] V. Everts, E. van der Zee, L. Creemers, W. Beertsen, Phagocytosis and intracellular digestion of collagen, its role in turnover and remodelling, Histochem. J. 28 (1996) 229–245.

[4] M.T. van der Pauw, T. Van den Bos, V. Everts, W. Beertsen, Phagocytosis of fibronectin and collagens type I, III, and V by human gingival and periodontal ligament fibroblasts in vitro, J. Periodontol. 72 (2001) 1340–1347.

[5] I. Takahashi, M. Nishimura, K. Onodera, J.W. Bae, H. Mitani, M. Okazaki, Y. Sasano, Expression of MMP-8 and MMP-13 genes in the periodontal ligament during tooth movement in rats, J. Dent. Res. 82 (2003) 646–651.

[6] M. Tsubota, Y. Sasano, I. Takahashi, M. Kagayama, H. Shimauchi, Expression of MMP-8 and MMP-13 mRNAs in rat periodontium during tooth eruption, J. Dent. Res. 81 (2002) 673–678.

[7] A.L. Bolcato-Bellemin, R. Elkaim, A. Abehsera, J.L. Fausser, Y. Haikel, H. Tenenbaum, Expression of mRNAs encoding for alpha and beta integrin subunits, MMPs, and TIMPs in stretched human periodontal ligament and gingival fibroblasts, J. Dent. Res. 79 (2000) 1712–1716.

[8] W. Beertsen, V. Everts, A. van den Hooff, Fine structure and possible function of cells containing leptomergic organelles in the periodontal ligament of the rat incisor, Arch. Oral Biol. 19 (1974) 1099–1100.

[9] W. Beertsen, V. Everts, The site of remodeling of collagen in the periodontal ligament of the mouse incisor, Anat. Rec. 189 (1977) 479–497.

[10] S. Takeshita, R. Kikuno, K. Tezuka, E. Amann, Osteoblast-specific factor 2: cloning of a putative bone adhesion protein with homology with the insect protein fasciclin I, Biochem. J. 294 (Pt. 1) (1993) 271–278.

[11] T. Sugiura, H. Takamatsu, A. Kudo, E. Amann, Expression and characterization of murine osteoblast-specific factor 2 (OSF-2) in a baculovirus expression system, Protein Expr. Purif. 6 (1995) 305–311.

[12] K. Horiuchi, N. Amizuka, S. Takeshita, H. Takamatsu, M. Katsuura, H. Ozawa, Y. Toyama, L.F. Bonewald, A. Kudo, Identification and characterization of a novel protein, periostin, with restricted expression to periosteum and periodontal ligament and increased expression by transforming growth factor beta, J. Bone Miner. Res. 14 (1999) 1239–1249.

[13] Y. Hirose, H. Suzuki, N. Amizuka, J. Shimomura, Y. Kawano, K. Nozawa-Inoue, A. Kudo, T. Maeda, Immunohistochemical localization of periostin in developing long bones of mice, Biomed. Res. 24 (2003) 31–37.

[14] H. Suzuki, N. Amizuka, I. Kii, Y. Kawano, K. Nozawa-Inoue, A. Suzuki, H. Yoshie, A. Kudo, T. Maeda, Immunohistochemical localization of periostin in tooth and its surrounding tissues in mouse mandibles during development, Anat. Rec. (2004).

[15] I. Kii, N. Amizuka, S. Kitajima, M. Li, K. Takeuchi, T. Maeda, J. Kanno, T. Inoue, Y. Saga, A. Kudo, Mechanical stress dependent remodeling of the periodontal ligament is defective in periostin deficient mice: mechanotransduction through periostin protein, J. Bone Miner. Res. 19 (Suppl. 1) (2004) s21.

[16] N. Amizuka, H.S. Lee, M.Y. Kwan, A. Arazani, H. Warshawsky, G.N. Hendy, H. Ozawa, J.H. White, D. Goltzman, Cell-specific expression of the parathyroid hormone (PTH)/PTH-related peptide receptor gene in kidney from kidney-specific and ubiquitous promoters, Endocrinology 138 (1997) 469–481.

[17] J. Wilde, M. Yokozeki, K. Terai, A. Kudo, K. Moriyama, The divergent expression of periostin mRNA in the periodontal ligament during experimental tooth movement, Cell Tissue Res. 312 (2003) 345–351.

[18] E. Afanador, M. Yokozeki, Y. Oba, Y. Kitase, T. Takahashi, A. Kudo, K. Moriyama, Messenger RNA expression of periostin and Twist transiently decrease by occlusal hypofunction in mouse periodontal ligament, Arch. Oral Biol. 50 (2005) 1023–1031.

[19] E. Hanssen, B. Reinboth, M.A. Gibson, Covalent and non-covalent interactions of betaig-h3 with collagen VI. Beta ig-h3 is covalently attached to the amino-terminal region of collagen VI in tissue microfibrils, J. Biol. Chem. 278 (2003) 24334–24341.

[20] K. Hashimoto, M. Noshiro, S. Ohno, T. Kawamoto, H. Satakeda, Y. Akagawa, K. Nakashima, A. Okimura, H. Ishida, T. Okamoto, H. Pan, M. Shen, W. Yan, Y. Kato, Characterization of a cartilage-derived 66-kDa protein (RGD-CAP/beta ig-h3) that binds to collagen, Biochim. Biophys. Acta 1355 (1997) 303–314.

[21] L. Gillan, D. Matei, D.A. Fishman, C.S. Gerbin, B.Y. Karlan, D.D. Chang, Periostin secreted by epithelial ovarian carcinoma is a ligand for alpha(V)beta(3) and alpha(V)beta(5) integrins and promotes cell motility, Cancer Res. 62 (2002) 5358–5364.

[22] R. Shao, S. Bao, X. Bai, C. Blanchette, R.M. Anderson, T. Dang, M.L. Gishizky, J.R. Marks, X.F. Wang, Acquired expression of periostin by human breast cancers promotes tumor angiogenesis through up-regulation of vascular endothelial growth factor receptor 2 expression, Mol. Cell. Biol. 24 (2004) 3992–4003.

[23] S. Bao, G. Ouyang, X. Bai, Z. Huang, C. Ma, M. Liu, R. Shao, R.M. Anderson, J.N. Rich, X.F. Wang, Periostin potently promotes metastatic growth of colon cancer by augmenting cell survival via the Akt/PKB pathway, Cancer Cell 5 (2004) 329–339.

[24] J.E. Kim, S.J. Kim, B.H. Lee, R.W. Park, K.S. Kim, I.S. Kim, Identification of motifs for cell adhesion within the repeated domains of transforming growth factor-beta-induced gene, betaig-h3, J. Biol. Chem. 275 (2000) 30907–30915.

[25] J.E. Kim, H.W. Jeong, J.O. Nam, B.H. Lee, J.Y. Choi, R.W. Park, J.Y. Park, I.S. Kim, Identification of motifs in the fasciclin domains of the transforming growth factor-beta-induced matrix protein betaig-h3 that interact with the alphavbeta5 integrin, J. Biol. Chem. 277 (2002) 46159–46165.

[26] H. Kudo, N. Amizuka, K. Araki, K. Inohaya, A. Kudo, Zebrafish periostin is required for the adhesion of muscle fiber bundles to the myoseptum and for the differentiation of muscle fibers, Dev. Biol. 267 (2004) 473–487.

[27] G.M. Dubois, Z. Haftek, C. Crozet, R. Garrone, D. Le Guellec, Structure and spatio temporal expression of the full length DNA complementary to RNA coding for alpha2 type I collagen of zebrafish, Gene 294 (2002) 55–65.

[28] A.P. Summers, T.J. Koob, The evolution of tendon–morphology and material properties, Comp. Biochem. Physiol. A Mol. Integr. Physiol. 133 (2002) 1159–1170.

[29] T.J. Koob, A.P. Summers, Tendon–bridging the gap, Comp. Biochem. Physiol. A Mol. Integr. Physiol. 133 (2002) 905–909.

ELSEVIER

EXPERIMENTAL HEMATOLOGY

Experimental Hematology 34 (2006) 1687–1697

Thioredoxin overexpression in mice, model of attenuation of oxidative stress, prevents benzene-induced hemato-lymphoid toxicity and thymic lymphoma

Guang-Xun Li[a,†], Yoko Hirabayashi[a,†], Byung-Il Yoon[a,*], Yasushi Kawasaki[a], Isao Tsuboi[a], Yukio Kodama[a], Yuji Kurokawa[a], Junji Yodoi[b], Jun Kanno[a], and Tohru Inoue[c]

[a]*Division of Cellular and Molecular Toxicology, Biological Safety and Research Center, National Institute of Health Sciences, Tokyo, Japan;* [b]*Department of Biological Responses, Research Center for Immunodeficiency Virus, Institute for Virus Research, Kyoto University, Kyoto, Japan;* [c]*Biological Safety and Research Center, National Institute of Health Sciences, Tokyo, Japan*

(Received 6 March 2006; revised 10 July 2006; accepted 9 August 2006)

Objective. **Reactive oxygen species (ROS), generated following benzene exposure, are considered to trigger the development of hematopoietic neoplasms, although little supporting evidence has been found. In this study, we examined whether the experimental elimination of ROS generated following benzene exposure prevents the development of benzene-induced hematopoietic disorders to clarify the mechanism underlying the development of benzene-induced hematopoietic disorders.**

Methods. **C57BL/6 mice, overexpressing human thioredoxin (h-Trx-Tg), were used to examine the possible nullification of ROS induction following benzene exposure. The experimental group was exposed to 300 ppm benzene 6 hours/day, 5 days/week, for 26 weeks, and lifetime observation followed by molecular and histopathological examinations were carried out.**

Results. **The present study using h-Trx-Tg mice showed a complete suppression of the development of thymic lymphoma induced by benzene inhalation (0% in h-Trx-Tg vs 30% in wild-type (Wt) mice). This was associated with a 48% decrease in the incidence of clastogenic micronucleated reticulocyte induction in the h-Trx-Tg mice compared with the Wt control after 2 weeks of inhalation. As underlying mechanisms, the attenuation of oxidative stress was accompanied by a complete abrogation of hemato-lymphoid toxicity, as shown by the upregulation of the activity of superoxide-dismutase, and a consequently stable ROS level, as determined by cell sorting using 2′,7′-dichlorodihydrofluorescein diacetate, along with a significant attenuation of the overexpression of a cell cycle–dependent kinase inhibitor, p21.**

Conclusion. **The attenuation of benzene-induced oxidative stress and that of the consequent lymphomagenesis were observed for the first time, and these indicate a role of oxidative stress in benzene-induced clastogenesis and lymphomagenesis. (These attenuations were not seen in nonthymic lymphomas, and no leukemias developed in C57BL/6 used in this study.) During the constitutive overexpression of h-*Trx*, the expression of aryl-hydrocarbon receptor in h-Trx-Tg mice was downregulated, which may also contribute to the attenuation.** © **2006 International Society for Experimental Hematology. Published by Elsevier Inc.**

Benzene, a ubiquitous contaminant in the environment, is a volatile solvent released from petroleum products such as natural gas condensates or industrial intermediates [1], as well as from vehicular emissions [2] and cigarette smoke [3]. Epidemiological studies such as those of shoe workers are still the focus of much interest [4,5], and the impact of benzene at levels below the U.S. occupational standard of 1 part per million (ppm) makes risk characterization problematic [6]. Phenolic metabolites derived from cytochrome p450 2E1 (CYP2E1) rearranged via benzene oxide [7] are

Offprint requests to: Yoko Hirabayashi, M.D., Ph.D., Cellular and Molecular Toxicology Division, Center for Biological Safety and Research, National Institute of Health Sciences, 1-18-1 Kamiyohga, Setagayaku, Tokyo 158-8501, Japan; E-mail: yokohira@nihs.go.jp

*Present address: Department of Veterinary Medicine, College of Animal Resource, Kangwon National University, Kangwon-Do 200-701, Republic of Korea.

†Guang-Xun Li and Yoko Hirabayashi both contributed equally to this work.

0301-472X/06 $–see front matter.
doi: 10.1016/j.exphem.2006.08.005

considered to be generators of reactive oxygen species (ROS) after hydroxylation by myeloperoxidase, and the consequent oxidative stresses are further considered to induce acute hemato-lymphoid toxicity in the bone marrow (BM) [8,9]. However, the mechanism underlying lympho/leukemogenicity remains unclarified, because the Ames revertant mutagenesis assay of benzene and its major metabolites is known to yield negative results [10,11] and neither sufficient DNA binding nor a significant amount of adduct formation is observed [12,13], probably owing to the less electrophilic nature of benzene and its metabolites [14]. Hence, previous studies on the induction of ROS during benzene metabolism only focused on other types of genotoxic damage. Other types of chromosomal damage including clastogenic micronucleic reticulocyte formation [15] induced by ROS and benzene and its metabolites, namely, hydroquinone, catechol, and *trans-trans*-muconic acid, are assumed to be the consequences of genotoxicities [16]. This may be in good agreement with the observed severe benzene toxicity in p53-knockout (KO) mice. However, there has been no direct in vivo evidence, and only a few in vitro studies indicating that an increase in the rate of homologous recombination initiated by benzene monoxide induces oxidative stress have been reported [17]. Because thioredoxin (Trx) might protect mice against oxidative stress following benzene exposure, genetically modified Trx mice, specifically transgenic Trx mice, were used to support the above-mentioned contention.

Genetically modified mice, namely Trx-KO mice and Trx-overexpressing (Tg) mice, respond to ROS in a *Trx* gene-dosage-dependent manner. Human (h) Trx-Tg mice were used in the present study to resolve the above controversy, because h-Trx-Tg mice are tolerant to oxidative stress [18–20] and may elucidate whether oxidative stress is a major trigger of benzene-induced hematopoietic neoplasms in vivo. The exacerbation of benzene-induced hemato-lymphoid toxicity in Trx-KO ($Trx^{+/-}$) mice and the attenuation of that in h-Trx-Tg mice confirm, for the first time, that the hemato-lymphoid toxicity is caused by oxidative stress at the whole-animal level. Furthermore, although nonthymic lymphoma was not suppressed, benzene-induced thymic lymphomagenesis was inhibited 100% in h-Trx-Tg mice, and the mechanism underlying benzene-induced lymphomagenesis was also elucidated to involve oxidative stress.

Materials and methods

Experimental animals

h-Trx-Tg, $Trx^{+/-}$, and wild-type (Wt) mice were maintained in the board-approved laboratory animal facility of the National Institute of Health Sciences (NIHS) of Japan. The h-Trx-Tg and Trx-KO C57BL/6 mice were originally bioengineered by Mitsui et al. [19] and Matsui et al. [21], respectively. Because the homozygousity for Trx KO is embryonic lethal, $Trx^{+/-}$ mice were used in this study. Both $Trx^{+/-}$ mice and h-Trx-Tg mice were maintained in heterozygosity and their genotypes were confirmed at the weaning stage by the polymerase chain reaction (PCR) screening of DNA from the tail of each mouse. The expression levels of the endogenous murine (m)*Trx* gene, during the steady state of Wt mice, h-Trx-Tg mice, and $Trx^{+/-}$ mice, three of each, used in the present study are shown in Figure 1. In the $Trx^{+/-}$ mice, because the mice are Trx hemizygous KO, the m-*Trx* expression level was nearly one-half in allelic number that in Wt mice, whereas h-Trx-Tg mice showed the same expression level as that in Wt steady-state mice.

Benzene

Benzene, Cas. No. 71-43-2, MW 78.11, was purchased from Wako Fine Chemical Company (Osaka, Japan).

Benzene exposure and dose monitoring

The mice were randomly assigned to groups and individually housed. They were exposed to benzene in 1.3m^3 inhalation chambers as described previously [22,23]. Briefly, benzene vapor was generated by heating liquid benzene to 16°C and directed into the inhalation chambers (Sibata Scientific Technology Ltd., Tokyo, Japan). The flow rate of benzene was about 650 L/min, and benzene concentration in the chambers was measured at 30-minute intervals during daily exposures using a gas chromatograph (Shimadzu Co., Kyoto, Japan). The temperature and humidity in the chambers were automatically controlled at 24°C ± 1°C and 55% ± 10%, respectively. The incoming air and exhaust air were passed through high-efficiency particulate-air filters.

For short-term exposure, the mice were divided into sham-exposed and benzene-exposed groups. Benzene was exposed to 300 ppm for 6 hours/day, 5 days/week for 2 weeks. The sham-exposed mice were maintained under the same conditions as the benzene-exposed group except for benzene inhalation.

For long-term exposure in the lymphomagenicity study, see later sections.

Peripheral blood parameters and BM cellularity

Peripheral blood from three mice of each genotype was collected from the orbital plexus, and blood parameters were measured using a Sysmex M-2000 blood cell counter (Sysmex Co., Osaka,

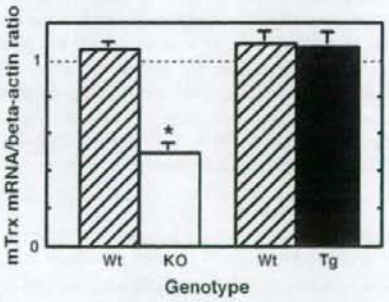

Figure 1. Steady-state murine (m)-*Trx* gene expressions of BM cells from three mice of each of endogenous $Trx^{+/-}$ (open column) and h-Trx-Tg mice (closed column), compared with those in littermate Wt mice (each paired hatched column). The ordinate (y axis) indicates the ratio of mRNA expression level of m-Trx to that of β-actin (*: $p < 0.05$).

Japan). BM cells from bilateral femurs of three mice of each genotype were harvested from the benzene-exposed and sham-exposed mice. Total and differential cell counts were also determined using a Sysmex M-2000.

In vitro colony assays

Colony-forming unit granulocyte-macrophages (CFU-GMs) were assayed in a semisolid methylcellulose culture medium [23,24]. Briefly, a mixture of 8×10^4 BM cells from three mice of each genotype were suspended in 4 mL of α-medium containing 0.8% methylcellulose (Nakalai Tesque, Co., Ltd., Kyoto, Japan), 30% fetal calf serum (HyClone Laboratories, Inc., Logan, UT, USA), 1% bovine serum albumin (Sigma, St. Louis, MO, USA), 10^{-4} M 2-mercaptoethanol (Sigma), and 10 ng/mL murine granulocyte-macrophage colony-stimulating factor (m-GM-CSF, R&D Systems, Inc., Minneapolis, MN, USA). One milliliter of methylcellulose medium containing this cell suspension was plated in 35-mm tissue culture wells in triplicate (Nalgen Nunc International, Naperville, IL, USA) and incubated in a humidified chamber at 37°C in 5% CO_2 for 6 days. Colonies were counted under an inverted microscope (Olympus, Tokyo, Japan).

Micronucleus analysis of peripheral blood

Acridine orange (AO)-coated glass slides (Toyobo, Kyoto, Japan) and peripheral blood cells were prepared as described previously [25]. A blood sample collected from the same three mice of each genotype at each time point (i.e., before and 3, 5, 10, 12, 15, and 18 days after benzene inhalation) was placed at the center of an AO-coated glass slide and covered with a 24 × 40-mm cover slip. Supravitally AO-stained reticulocytes were examined under a fluorescence microscope with a blue excitation filter and a yellow barrier filter. The frequency of micronucleated reticulocytes (MN-Rets) among 2000 cells per mouse was determined.

Assay of benzene-induced lymphomagenicity

For lymphomagenicity studies, the numbers of mice per groups, namely, Wt mice with or without benzene exposure, and Tg mice with or without benzene exposure, were 10 BWt mice, 8 CWt mice, 13 BTg mice, and 8 CTg mice, respectively. The mice were supplied water ad libitum, but food pellets were withdrawn during the exposure. For long-term exposure, the mice were divided into the sham-exposed control and the benzene-exposed groups. The latter group was exposed to 300 ppm benzene 6 hours/day, 5 days/week, for 26 weeks. The sham-exposed control group was maintained under the same conditions as the benzene-exposed group except for benzene inhalation. All the mice were monitored throughout their lifetime except for those showing symptoms of advanced hematopoietic neoplasms such as anemia and palpable splenomegaly; these were euthanized at the agonal period and then examined hematopathologically. The remaining mice were also examined histopathologically.

Histopathological examination

For the evaluation of hemopoietic malignancies caused by benzene inhalation in Wt and h-Trx-Tg mice, mice from each group were sacrificed under ethyl ether anesthesia for autopsy. For the histopathological examination, all the visceral organs including the thymus, spleen, sternum, and femoral BM were fixed in 10% neutral buffered formalin for 24 hours. The sternum and femoral BM were decalcified in 7.5% formic acid for 72 hours. After conventional processing, paraffin-embedded sections were stained with hematoxylin and eosin (H & E) and then examined histopathologically under a light microscope. The diagnostic definition of histopathological typing for lymphomagenesis was according to previous publications [26,27].

Reverse transcription and polymerase chain reaction

The expression of genes encoding murine and human Trx, $p21^{waf1}$, aryl hydrocarbon receptor (AhR), and CYP2E1 was evaluated by reverse transcription (RT) followed by a PCR technique. Total RNA from the BM cells of three mice of each genotype at each time point was isolated using a Qiagen RNAeasy kit (Qiagen, Valencia, CA, USA).

RT was performed using total RNA and random hexamers as primers with a reverse transcription kit from Applied Biosystems (Foster City, CA, USA). PCR amplification was performed using the following previously designed oligonucleotide primers [28]: For mouse AhR, forward primer 5′-GAT GCC TTG GTC TTC TAT-3′, reverse primer 5′-TCATGCCACTTTCTCCAGTCT-3′; for mouse $p21^{waf1}$, forward primer 5′-ATCTCCAATCCTGGTGATGT-3′, reverse primer 5′-TGCAGCAGGGCAGAGGAAGT-3′; for mouse CYP2E1, forward primer 5′-TGACTTTGGCCGA CCTGTTC-3′, reverse primer 5′-GAATCAGGAGCCCATATCT-3′.

The expression of murine and human Trx mRNAs was also quantitatively evaluated by real-time PCR using TaqMan with the Applied Biosystems 7900HT Sequence Detection System (Applied Biosystems). PCR conditions and data analysis were according to SDS ver.2.0. All of the samples were run in triplicate using the *glyceraldehyde-3-phosphate dehydrogenase* (*GAPDH*) gene as the standard gene, because *GAPDH* expression level does not change significantly across genotypes or with benzene exposure time, as shown in Figures 3, 7, and 10. For the quantitative evaluation of mRNA expression, the following four primers and corresponding probes were designed using computer software Primer Express ver. 1.5 (Applied Biosystems): For m-Trx mRNA, forward primer 5′-GGATGTTGCTGCAGACTGTGA-3′, reverse primer 5′-CCCCACCTTTTGACCCTTTT-3′, the probe 5′-FAM-TCAAATGCATGCCGACCTTCCAGTT-TAMRA-3′; for h-Trx mRNA, forward primer 5′-CCATTTCCATCGGTCCTTACA-3′, reverse primer 5′-GCTCTCGATCTGCTTCACCAT-3′, the probe 5′-FAM-CGCTCGTCAGACTCCAGCAGCCA-TAMRA-3′; for m-β-actin, forward primer 5′-GCTCTGGCTCCTAGCACCAT-3′, reverse primer 5′-GCCACCGATCCACACAGAGT-3′, the probe 5′-VIC-CAAGATCATTGCTCCTCCTGAGCGCA-TAMRA-3′; for m-GAPDH, forward primer 5′-TGTGTCCGTCGTGGATCTGA-3′, reverse primer 5′-CCTGCTTCACCACCTTCTTGA-3′, the probe 5′-VIC-CCGCCTGGAGAAACCTGCCAAGTATG-TAMRA-3′.

Western blot analysis

Total protein (15 μg) from BM cells of three mice of each genotype was electrophoresed in a 15% SDS-polyacrylamide gel. Separated proteins were transferred to a nitrocellulose membrane (Hybond-ECL; Amersham, Arlington Heights, IL, USA). The p21 protein was visualized by immunostaining with a rabbit anti-mouse p21 polyclonal antibody (Santa Cruz Biotechnology, Inc., Santa Cruz, CA, USA) and an anti-rabbit-HRP-conjugated anti-rabbit p21 polyclonal antibody (Santa Cruz Biotechnology) in ECL detection reagent (ECL, RPN 2209) (Amersham Life Science, CA, USA).

Assay of superoxide dismutase activity of BM

The total Cu/Zn and Mn superoxide dismutase (SOD) activity was determined essentially using the method described by Fridovich [29]. An SOD assay kit (Wako, Osaka, Japan) was used for the quantification of total SOD activity. SOD activity was determined from the percentage inhibition of xanthine-xanthine oxidase-reduced nitroblue tetrazolium (NTB). Briefly, BM cells from three mice of each genotype were lysed in 0.1% Triton X, subjected to two freeze/rethaw cycles, and then stored on ice. The increase in absorbance at 560 nm was monitored at 37°C for 20 minutes using a spectrophotometer (Beckman DU-600, Beckman Coulter, Inc., Fullerton, CA, USA).

Measurement of erythrocyte ROS production

In the assessment of the attenuation of benzene-induced ROS production in the h-Trx-Tg mice, we loaded erythrocytes from the same three mice of each genotype at each time point with a 20-μM fluorescent probe, 2′,7′-dichlorodihydrofluorescein diacetate (DCFH-DA, Sigma, St. Louis, MO, USA), and analyzed intracellular fluorescence intensity by flow cytometry [30–32]. Briefly, peripheral blood (5 μL) was obtained from the mouse tail. Blood was washed once and diluted with Ca^{2+}- and Mg^{2+}-free Dulbecco's phosphate-buffered saline (D-PBS) (Invitrogen Corp., Carlsbad, CA, USA) to a concentration of 1×10^6 cells/mL. To this preparation, 20 μM DCFH-DA dye was added after incubation at 37°C for 15 minutes in a humidified atmosphere of 5% CO_2. The obtained red blood cell (RBC) suspension was washed with D-PBS. RBCs were obtained using a fluorescence-activated cell sorter (FACS-Calibur, Becton-Dickinson, San Francisco, CA, USA). A typical experiment included untreated control cells for establishing a baseline, and cells treated with 100 μM paraquat (Tokyo Kasei, Tokyo, Japan) as the positive control, which were incubated at 37°C in a humidified atmosphere of 5% CO_2 for 25 minutes to induce ROS production. A gate was set to include only erythrocytes and to exclude reticulocytes, nucleated RBCs (normoblasts), and white blood cells. A 488-nm argon laser beam was used for excitation. The histograms and dot-plotted mean fluorescence intensity were analyzed using Cell Quest software (Beckman Coulter, Inc.) [33,34].

Statistical analyses

Statistical comparisons were performed by the analysis of variance (ANOVA) (ANOVAM: Ver.0.04, Seoul, Korea). To determine the statistical significance of difference, quantitative PCR data were subjected to single-tailed Student's *t*-test. Significant differences between groups were determined by two-way ANOVA ($p < 0.05$). All of the data are presented as the mean ± standard error of the mean.

Results

Effect of benzene toxicity on blood parameters according to Trx genotype

Benzene exposure for 6 hours/day, 5 days/week, for 2 weeks decreased the percentage of white blood cells in peripheral blood and the percent cellularities of femoral BM cells in the Wt controls as indicated by hatched columns in Figure 2A (57.1% and 52.2% for white blood cells; 68.0% and 61.0% for the BM cells, respectively, with respect to the sham-exposed controls expressed as 100%). These results are comparable to those of a previous report [23]. In the h-Trx-Tg mice (solid columns), the decreases were statistically significantly attenuated as compared with those in the Wt groups (each hatched column) (91.2% vs 52.2% for white blood cells, $p < 0.05$, and 87.0% vs 61.0% for BM cells, $p < 0.05$; with respect to each sham-exposed group). Whereas lymphocyte counts in Wt mice decreased specifically after benzene exposure from 50.6 ± 3.0 to 11.8 ± 1.4 × 10^2/μL (i.e., decreased to 23.3% of control), the Tg mice showed no significant decrease in white blood cell (WBC) count, and the decrease in lymphocyte counts was also not significant (43.7 ± 1.9 to 41.9 ± 1.1 × 10^2/μL). In the $Trx^{+/-}$ mice (open columns in this figure), although benzene toxicity in this group was supposed to be exaggerated, the decreases were not significantly different from those in Wt mice (hatched columns) (75.0% vs 57.1% for white blood cells and 61.5% vs 68.0% for BM cells; with respect to each sham-exposed group). Thus, the hemizygous Trx deficiency may not be significantly insufficient for induction of benzene-mediated BM toxicity. Statistically less significant decreases in the percentage of RBCs observed in the Wt, h-Trx-Tg, and $Trx^{+/-}$ mice (hatched, solid, and open columns, respectively) might be due to the early observation of prolonged anemia.

Figure 2B shows the comparison of the percentage of hemopoietic progenitor cells, CFU-GMs, after benzene exposure between the $Trx^{+/-}$ mice and Wt mice (left), and that

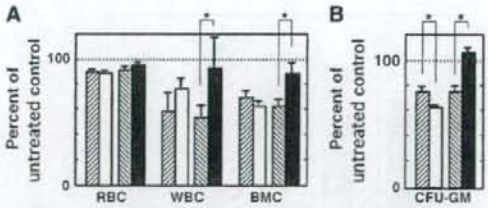

Figure 2. **(A)** Changes in peripheral blood parameters from three mice of each genotype, namely, the percentage numbers of red blood cells (RBCs) and white blood cells (WBCs), and bone marrow cellularity (BMC), after benzene exposure, for 6 h/d, 5d/wk, for 2 weeks. Open columns indicate $Trx^{+/-}$ mice; solid columns, h-Trx-Tg mice; compared with Wt mice, hatched columns. All the columns indicate % of sham-exposed control mice of each genotype. Note that experiments using $Trx^{+/-}$ and h-Trx-Tg mice were conducted separately with Wt mice in each littermate, and are thus indicated by hatched columns in opposite directions. **(B)** Changes in percentage number of CFU-GMs after benzene exposure for 6 h/d, 5 d/wk, for 2 weeks. A mixture of BM cells from three mice of each genotype was used. Open column indicates $Trx^{+/-}$ mice, which show a marked decrease in the percentage number of CFU-GMs as compared with the benzene-exposed Wt mice (hatched column on the far left). The h-Trx-Tg mice (solid column) showed no changes in percentage relative to the sham-exposed h-Trx-Tg mice, whereas the benzene-exposed Wt mice (hatched column, second from the right) showed a significant decrease.